

JYX



This is a self-archived version of an original article. This version may differ from the original in pagination and typographic details.

Author(s): Pavlyukh, Yaroslav; Stefanucci, Gianluca; van Leeuwen, Robert

Title: Dynamically screened vertex correction to GW

Year: 2020

Version: Published version

Copyright: ©2020 American Physical Society

Rights: In Copyright

Rights url: <http://rightsstatements.org/page/InC/1.0/?language=en>

Please cite the original version:

Pavlyukh, Y., Stefanucci, G., & van Leeuwen, R. (2020). Dynamically screened vertex correction to GW. *Physical Review B*, 102(4), Article 045121.

<https://doi.org/10.1103/PhysRevB.102.045121>

Dynamically screened vertex correction to GW Y. Pavlyukh **Institut für Physik, Martin-Luther-Universität Halle-Wittenberg], 06120 Halle, Germany*G. Stefanucci *Dipartimento di Fisica, Università di Roma Tor Vergata, Via della Ricerca Scientifica 1, 00133 Rome, Italy*R. van Leeuwen *Department of Physics, Nanoscience Center, University of Jyväskylä, FI-40014 Jyväskylä, Finland*

(Received 6 April 2020; revised 16 June 2020; accepted 23 June 2020; published 15 July 2020)

Diagrammatic perturbation theory is a powerful tool for the investigation of interacting many-body systems, the self-energy operator Σ encoding all the variety of scattering processes. In the simplest scenario of correlated electrons described by the GW approximation for the electron self-energy, a particle transfers a part of its energy to neutral excitations. Higher-order (in screened Coulomb interaction W) self-energy diagrams lead to improved electron spectral functions (SFs) by taking more complicated scattering channels into account and by adding corrections to lower order self-energy terms. However, they also may lead to unphysical negative spectral functions. The resolution of this difficulty has been demonstrated in our previous works. The main idea is to represent the self-energy operator in a Fermi golden rule form which leads to a manifestly positive definite SF and allows for a very efficient numerical algorithm. So far, the method has only been applied to the three-dimensional electron gas, which is a paradigmatic system, but a rather simple one. Here we systematically extend the method to two dimensions including realistic systems such as monolayer and bilayer graphene. We focus on one of the most important vertex function effects involving the exchange of two particles in the final state. We demonstrate that it should be evaluated with the proper screening and discuss its influence on the quasiparticle properties.

DOI: [10.1103/PhysRevB.102.045121](https://doi.org/10.1103/PhysRevB.102.045121)**I. INTRODUCTION**

Numerous correlated electron calculations follow a canonical scheme formulated by Hedin [1] in terms of dressed propagators. It is now well established that the lowest-order self-energy (SE) term, the so-called GW approximation, is the major source of electronic correlations. Much less is known about the next perturbative orders: there is no single standard way of evaluating them despite the fact that there is a single second-order self-energy diagram (Fig. 1). There are multiple reasons for this. On one side, at the advent of many-body perturbation theory (MBPT) the computational power was insufficient to perform these demanding calculations, and one was forced to use some drastic simplifications. On the other side, there are several conceptual problems with the organization of many-body perturbation theory (MBPT) for interacting electrons. For instance, it is known that higher-order diagrammatic approximations for the electron self-energy in terms of the screened Coulomb interaction W leads to poles in the “wrong” part of the complex plane giving rise to *negative spectral densities*. This observation has been made a long time ago by Minnhagen [2,3], and in our recent works we provided a general solution to this problem [4,5] yielding positive

definite (PSD) spectral functions. The idea was to write the self-energy in the Fermi golden rule form well known from scattering theory.

One interesting conclusion of our theory is that the second-order SE describes three distinct scattering processes that take place in a many-body system [6]: (I) A correction to the first-order scattering, involving the same final states as in GW . This effect was numerically studied in Ref. [4], and has been shown [6] to counteract the smearing out of spectral features in self-consistent calculations [7]. (II) Excitation of two plasmons (pl), or two particle-hole pairs ($p-h$), or a mixture of them in the final state. Especially the generation of two plasmons is a prominent effect spectroscopically manifested as a second satellite in the photoemission spectrum [8]. This effect can be obtained from the cumulant expansion [9,10], inspired by the electron-boson model [11,12]. (III) A first-order scattering involving the exchange of the two final state particles. This latter scattering process is the focus of the present work.

Some manifestations of mechanism (III) have already been studied, albeit without realizing its deep connection with the full $\Sigma^{(2)}$. First of all, for the two *bare* interaction lines we get the so-called *second-order exchange* contribution, which has been shown to play an important role in correlated electronic calculations for molecular systems as an ingredient of the second-Born approximation (2BA) [13–15]. Second, it yields a very important total energy correction for the homogeneous

*yaruslav.pavlyukh@gmail.com

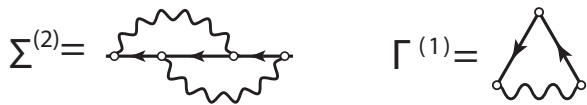


FIG. 1. A single second-order self-energy diagram and the associated first-order vertex function in terms of the electron propagators (arrows) and the screened interactions (wavy lines).

electron gas [16]. Third, the mechanism *with screening* has been considered in the calculations of quasiparticle lifetimes. Reizer and Wilkins predicted that this diagram yields a 50% reduction of the scattering rate in the two-dimensional (2D) electron gas calling it “a nongolden-rule” contribution, whereas Qian and Vignale [17] correctly pointed out that it is “still described by the Fermi golden rule, provided one recognizes that the initial and final states are Slater determinants,” and that the coefficient is different. Fourth, the mechanism is relevant for the scattering theory [18]. With bare Coulomb interactions it represents the so-called double photoemission (DPE) process, and if the interaction is screened—the plasmon assisted DPE [19,20]. Finally, the considered mechanism has some features in common with the second-order screened exchange (SOSEX) approximation [21,22]. However, there are also important differences in the constituent screened Coulomb interaction that will be explained below.

As can be seen from this list, the mechanism underlies various physical processes. However, it has not been sufficiently emphasized that all of them can be derived from a single $\Sigma^{(2)}$ diagram. Moreover, there are no systematic studies of its impact on the quasiparticle properties other than the lifetimes. These gaps are filled in here. Our theoretical derivations are illustrated by calculations for four prominent systems: the homogeneous electron gas in two and three dimensions and the mono- and bilayer graphene. While the former two are very well studied model systems [23,24], graphene is a real material, and while the *GW* calculations for it exists [25–27], MBPT has mostly been used in the renormalization group sense [28]. Little is known about the frequency dependence of higher-order self-energies.

Our approach consists of analytical and numerical parts. For the quasiparticle (*qp*) electron Green’s function (G_0) and the screened interaction (W_0) in the random phase approximation (RPA), the frequency integration of a selected set of the electron self-energy ($\Sigma[G_0, W_0]$) diagrams is performed in closed form using our symbolic algorithm implemented in the MATHEMATICA computer algebra system. The remaining momentum integrals are performed numerically in line with our previous studies using the Monte Carlo approach [4–6,29] showing excellent accuracy and scalability. First, we evaluate the scattering rate function

$$\Gamma(k, \omega) = i[\Sigma_c^>(k, \omega) - \Sigma_c^<(k, \omega)], \quad (1)$$

and then the retarded self-energy via the Hilbert transform (Appendix A)

$$\Sigma^R(k, \omega) = \Sigma_x(k) + \int \frac{d\omega'}{2\pi} \frac{\Gamma(k, \omega')}{\omega - \omega' + i\eta}, \quad (2)$$

where $\Sigma_x(k)$ is the frequency-independent exchange self-energy, and the meaning of greater $>$ and lesser $<$ compo-

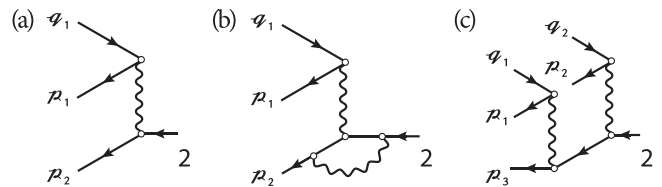


FIG. 2. Half-diagrams for $D(2)$, the constituent of the $\Sigma^{<(1, 2)}$ SE. All vertices are on the C^+ branch. Wavy lines stand for the screened interaction W .

nents of the correlated self-energy Σ_c is explained in the next section. Via the Dyson equation (Appendix E), the retarded self-energy determines correlated electronic structure.

Our work is structured as follows: we review our PSD approach in Sec. II and illustrate it with a concrete set of diagrams in Sec. III. Next we discuss the building blocks of our diagrammatic perturbation theory and provide reference G_0W_0 calculations for the four systems in Sec. IV. Efficient evaluation of screening is an important ingredient. In Sec. V we present our main numerical results: spectral features in $\Sigma^{(2)}$, cancellations between the first- and the second-order self-energies in the asymptotic regime, and quasiparticle properties such as quasiparticle peak strengths, effective masses, velocities, and lifetimes. We finally present our conclusions and outlooks in Sec. VI.

II. SUMMARY OF THE PSD APPROACH

Besides numerical difficulties, the major reason why the MBPT calculations for the electron gas have not been systematically performed at higher orders is the fact that the resulting expansions do not generate positive definite (PSD) spectral functions at all frequency and momentum values. How to deal with this obstacle is discussed in detail in Refs. [4,5].

Even though this is an equilibrium problem, our method can most easily be formulated by using the nonequilibrium Green’s function (NEGF) formalism [30]. The main distinction is that field operators [$\hat{\psi}(\mathbf{x}, z)$ and $\hat{\psi}^\dagger(\mathbf{x}, z)$ for electrons] evolve on the time-loop contour $z \in \mathcal{C}$ with one forward chronologically ordered (C^-) branch and one (C^+) branch with antichronological time ordering, $\mathcal{C} = C^- \cup C^+$. Correspondingly, the two times Green’s functions generalize to $G(\mathbf{x}_1 z_1, \mathbf{x}_2 z_2)$ or $G^{\alpha\beta}(\mathbf{x}_1 t_1, \mathbf{x}_2 t_2)$, where t_1 and t_2 are the projections of $z_{1,2}$ on the real-time axis, and $\alpha, \beta = +/-$ indicate to which branches of the Keldysh contour they belong. In the following, we will explicitly deal with the *lesser* self-energy $\Sigma^< \equiv \Sigma^{+-}$, which describes scattering processes on the subspace of states below the Fermi level, i.e., holes. The *greater* component ($\Sigma^> \equiv \Sigma^{+-}$) can be treated analogously.

The PSD property concerns the fact that the rate operator (1) must be positive for all momentum k and frequency ω values. Σ_c with this property is diagrammatically constructed starting from any given set of diagrams as follows.

In the first step pluses and minuses are assigned to the diagram vertices in all possible combinations. They carry information about the contour times. The resulting decorated diagrams are called *partitions*. Since we have shown that at zero temperature no isolated $+$ or $-$ islands can exist [4], the

“cutting” procedure splits the diagrams for $\Sigma_c^<$ into halves that have their vertices exclusively either on the $(-)$ or on the $(+)$ branch (viz. Fig. 2). They are the building blocks of the PSD construction. Subsequently, the half-diagrams are combined in such a way that a sum of complete squares is formed. This guarantees the positivity of the resulting set of diagrams. In the language of scattering theory, the half-diagrams have the meaning of S matrices describing various particle or hole scattering processes in a many-body system. The resulting PSD self-energies have then the Fermi golden rule form, which always leads to positive scattering rates. Topologically distinct S matrices will be denoted as D diagrams. Diagrams that can be obtained by the cutting procedure applied to Σ_c of the first and second order in W_0 are depicted in Fig. 2.

They are interpreted according to the standard diagrammatic rules. Consider for instance the half-diagrams with all the time arguments on the $+$ branch (such as depicted in Fig. 2). In addition to the initial one-hole ($1h$) state [with the coordinate 2, where the composite position-spin and time variables are abbreviated as $i \equiv (\mathbf{x}_i, t_i)$], the final state is denoted by the two strings of numbers $\underline{\rho} = (\rho_1, \dots, \rho_N, \rho_{N+1})$ and $\underline{q} = (q_1, \dots, q_N)$ that specify composite coordinates of the outgoing $N + 1$ holes and N particles, respectively. We further associate a single time-argument τ with $(\underline{\rho}, \underline{q})$. τ is the latest time on the forward and the earliest time on the backward contour branches. With these notations, $D^{(a)}$ reads

$$D_{\rho_1, \rho_2, q_1}^{(a)}(2) = -(-1)^1 \int d(4) W_0^{++}(4, 2) g^<(\rho_2 \tau, 2) \times g^<(\rho_1 \tau, 4) g^>(4, q_1 \tau), \quad (3a)$$

and its complex conjugate is given by

$$[D_{\rho_1, \rho_2, q_1}^{(a)}(1)]^* = + \int d(3) W_0^{--}(1, 3) g^<(1, \rho_2 \tau) \times g^<(3, \rho_1 \tau) g^>(q_1 \tau, 3), \quad (3b)$$

where the extra minus sign $(-1)^1$ in Eq. (3a) is due to the fact that for each time integration associated with a vertex on \mathcal{C}^+ :

$$\int_{\mathcal{C}^+} dz_i \dots = - \int_{-\infty}^{\infty} dt_i \dots \quad (4)$$

Equations (3) are expressed in terms of the bare electron propagators $g(\mathbf{x}_1, t_1; \mathbf{x}_2, t_2)$ and the RPA screened interaction

$$W_0(1, 2) = \int d(3) v(1, 3) \varepsilon_0^{-1}(3, 2), \quad (5)$$

where ε_0 is the RPA dielectric function defined in terms of the polarization bubble \mathcal{P}_0 and the bare Coulomb interaction v ,

$$\varepsilon_0(1, 2) = \delta(1, 2) - \int d(3) v(1, 3) \mathcal{P}_0(3, 2), \quad (6)$$

$$\mathcal{P}_0(1, 2) = -ig(1, 2)g(2, 1). \quad (7)$$

In Eqs. (3) $W_0^{--} \equiv W_0^T$ and $W_0^{++} \equiv W_0^{\bar{T}}$ stand for the *time-ordered* and *anti-time-ordered* interactions, respectively. We refer to Appendix B for the detailed definitions and Sec. IV for explicit forms of the dielectric function for the four studied systems. $D^{(b)}$ and $D^{(c)}$ are defined analogously. Our next goal is to describe self-energies that are obtained by “gluing” the

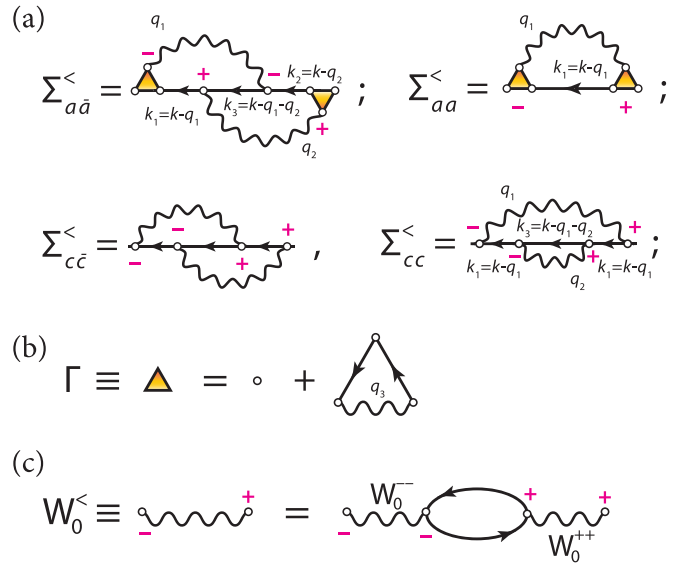


FIG. 3. (a) The contributions to $\Sigma_{\text{PSD}}^<$ given by Eq. (8) and arising from the first- and second-order (in screened interaction) self-energy by virtue of the PSD procedure (Sec. II). Three subsets of these diagrams that also fulfill the PSD property are given by Eqs. (A4). (b) First-order vertex function Γ . (c) Random phase approximation for the lesser component of the screened Coulomb interaction.

D diagrams. This is complementary to our earlier works [4,5], where the half-diagrams were derived by the cutting rules.

III. SELF-ENERGY APPROXIMATIONS: PHYSICAL MEANING OF DIAGRAMS

It is straightforward to see that by gluing three half-diagrams $D^{(i)}(2)$ ($i = a, b, c$, Fig. 2) with their complex conjugates $[D^{(i)}(1)]^*$ with or without permutations of internal coordinates, one obtains the four classes shown in Fig. 3(a). They are grouped into three terms covering three distinct physical mechanisms:

$$\Sigma_{\text{PSD}}^<(1, 2) = \Sigma_{aa}^<(1, 2) + [\Sigma_{cc}^<(1, 2) + \Sigma_{cc}^<(1, 2)] + \Sigma_{aa}^<(1, 2). \quad (8)$$

In Ref. [4] we have also shown that this is the *minimal set* of diagrams covering all the first- and second-order self-energies and possessing the PSD property. Let us discuss the involved physical mechanisms and derive the working formulas.

A. $\Sigma_{aa}^<$

$\Sigma_{aa}^<$ without vertex corrections is nothing else than the first-order (GW) self-energy. It results from gluing the simplest half-diagram $D^{(a)}$ [Fig. 2(a)] with itself without permuting the two hole lines (ρ_1 and ρ_2):

$$\Sigma_{GW}^<(1, 2) = i \sum_{\rho_1, \rho_2, q_1} [D_{\rho_1, \rho_2, q_1}^{(a)}(1)]^* D_{\rho_1, \rho_2, q_1}^{(a)}(2) = ig^<(1, 2)W_0^<(1, 2). \quad (9)$$

In order to establish the second equality, we use the explicit form of the half-diagrams (3), recall that $ig^<(1, 2) = \sum_{\rho_2} g^<(1, \rho_2 \tau) g^<(\rho_2 \tau, 2)$, $ig^<(3, 4) = \sum_{\rho_1} g^<(3, \rho_1 \tau)$

$g^<(p_1\tau, 4)$, and $-ig^>(4, 3) = \sum_{q_1} g^>(4, q_1\tau)g^>(q_1\tau, 3)$, and that the lesser screened interaction can be written in the form

$$W_0^<(1, 2) = -\iint d(3, 4) W_0^{--}(1, 3) \mathcal{P}_0^<(3, 4) W_0^{++}(4, 2),$$

with $\mathcal{P}_0^<(3, 4) = -ig^<(3, 4)g^>(4, 3)$ as shown in Fig. 3(c).

Now we use the diagrams in momentum and frequency representation as indicated in Fig. 3, namely

$$\mathbf{k}_1 = \mathbf{k} - \mathbf{q}_1, \quad \mathbf{k}_2 = \mathbf{k} - \mathbf{q}_2, \quad \mathbf{k}_3 = \mathbf{k} - \mathbf{q}_1 - \mathbf{q}_2, \quad (10)$$

in order to derive a standard result for the GW self-energy:

$$\Sigma_{GW}^<(k, \omega) = i \int d\Omega_1 \int \frac{d\nu_1}{2\pi} g^<(k_1, \omega - \nu_1) W_0^<(q_1, \nu_1), \quad (11)$$

where $\int d\Omega_1 \equiv \int \frac{d^d q_1}{(2\pi)^d}$ denotes an integral over a d -dimensional momentum space, ω is the external frequency, and \mathbf{k} is the momentum. Since the electron gas is translationally and rotationally invariant, the electron self-energy depends only on the modulus $k = |\mathbf{k}|$, and the same holds true for all other single-particle quantities. For graphene systems, the integration additionally contains a sum over the bands and a respective scattering matrix element. We will generally use ω_i and \mathbf{k}_i for the energy and momentum of fermionic lines, and ν_i and \mathbf{q}_i for the interaction lines.

Introducing the spectral function of the screened interaction $C(q, \nu)$ and using explicit formulas for the bare propagators in Appendix B and in particular

$$g^<(k, \omega) = 2\pi n_F(k) \delta[\omega - \epsilon(k)], \quad (12)$$

$$W_0^<(q, \nu) = -2\pi i \theta(-\nu) C(q, -\nu), \quad (13)$$

where $n_F(k) \equiv n_F[\epsilon(k)]$ is the fermion occupation number, we obtain

$$\begin{aligned} \Sigma_{GW}^<(k, \omega) &= 2i\pi \int d\Omega_1 \int_0^\infty d\nu_1 n_F(k_1) C(q_1, \nu_1) \\ &\quad \times \delta(\omega + \nu_1 - \epsilon_1), \end{aligned} \quad (14)$$

with $\epsilon_i \equiv \epsilon(k_i)$. As long as the spectral function of neutral excitations is positive, $C(q, \nu) > 0$ (which is indeed the case because we use RPA for W_0 here [5]), the rate operator $[-i\Sigma_{GW}^<(k, \omega)]$ is positive too, as evident from Eq. (14), and the nature of the final scattering state is revealed: it consists of a hole with energy $\epsilon_1 - \nu_1$ and a neutral excitation such as a p - h pair or a plasmon with momentum q_1 and energy ν_1 .

Equation (9) can be extended by adding internal interaction lines to $D^{(a)}$ and maintaining the external indices and the way how the constituent half-diagrams are glued. The b -half-diagram depicted in Fig. 2(b) represents the simplest possibility

$$\begin{aligned} \Sigma_{aa}^<(1, 2) &= i \sum_{p_1, p_2, q_1} [D^{(a)} + D^{(b)}]_{p_1, p_2, q_1}^*(1) \\ &\quad \times [D^{(a)} + D^{(b)}]_{p_1, p_2, q_1}(2). \end{aligned} \quad (15)$$

$D^{(b)}$ has one extra interaction line and therefore by gluing it with $D^{(a)}$ leads to two equivalent terms of the second order in W_0 , and by gluing $D^{(b)}$ with itself to a term of third order. They

can conveniently be represented by introducing the vertex function Γ depicted as yellow triangle in Figs. 3(a) and 3(b) and familiar from the Hedin's functional equations [1,31]. If one starts from higher-order diagrams, the diagrammatic expansion of Γ becomes more complicated and starts to differ from the standard vertex function.¹ As in the case of Σ_{GW} , the electronic and the interaction lines connecting the + and - islands are given by the lesser propagators $g^<(k_1, \omega - \nu_1)$ and $W^<(q_1, \nu_1)$. In view of the energy conservation, only these two propagators depend on ν_1 , and the frequency integration can likewise be performed. It is clear that the same functional form proportional to $n_F(\omega + \nu_1) \delta(\omega - \epsilon_1 + \nu_1)$ is obtained. Therefore, we conclude that $D^{(b)}$ renormalizes the GW expression, but does not lead to new spectral features. Equation (15) is a complete square, therefore $\Sigma_{aa}^<(1, 2)$ is PSD. It was numerically evaluated in our earlier work [4].

B. $\Sigma_{cc}^<$ and $\Sigma_{cc}^<$

The same analysis can be applied to other diagrams. $\Sigma_{cc}^<$ and $\Sigma_{cc}^<$ feature the $--++$ partition (in this notation the vertices are traversed along the fermionic lines from 1 to 2 in the order opposite to arrows) and contain two diagrams from gluing the half-diagrams of the c type [Fig. 2(c)] $[D^{(c)}(1)]^*$ and $D^{(c)}(2)$ with and without permutation of the dangling fermionic lines, respectively:

$$\begin{aligned} \Sigma_{cc}^<(1, 2) + \Sigma_{cc}^<(1, 2) &= i \sum_{\underline{p}, \underline{q}} [D_{p_1, p_2, p_3, q_1, q_2}^{(c)}(1) \\ &\quad + D_{p_2, p_1, p_3, q_2, q_1}^{(c)}(1)]^* D_{p_1, p_2, p_3, q_1, q_2}^{(c)}(2). \end{aligned} \quad (16)$$

An explicit derivation of this expression in momentum-energy representation goes beyond the scope of this work. However, some physical insight can be gained by using the plasmon-pole approximation $C(q, \nu) = C(q) \delta[\nu - \Omega(q)]$ for the screened interaction (13). As can be seen from the diagrammatic representation (Fig. 3) of the self-energy (16), there are three lesser propagators connecting the + and - islands, which in the energy-momentum representation read $g^<(k_3, \omega - \nu_1 - \nu_2) W^<(q_1, \nu_1) W^<(q_2, \nu_2)$. In view of the energy conservation, these are the only propagators that depend on the frequencies $\nu_{1,2}$. Therefore, the integrals can be explicitly performed. A scattering process accompanied by the generation of two plasmons can be inferred from the resulting frequency dependence proportional to $n_F[\omega + \Omega(q_1) + \Omega(q_2)] \delta[\omega - \epsilon_3 + \Omega(q_1) + \Omega(q_2)]$, and is PSD per construction.

This scattering mechanism is manifested as a second plasmon satellite in the electron spectral function. Its diagrammatic treatment, especially within a self-consistent scheme, is numerically very difficult [6]. However, plasmonic satellites can be captured by the method of cumulant expansions [9,32] at reduced computational cost. Recently, a lot of activities

¹Since our theory maintains the Fermi golden rule form, Γ enters symmetrically unlike in the Hedin's theory. Not surprisingly, such an object was introduced in the context of photoemission by Almladh [18].

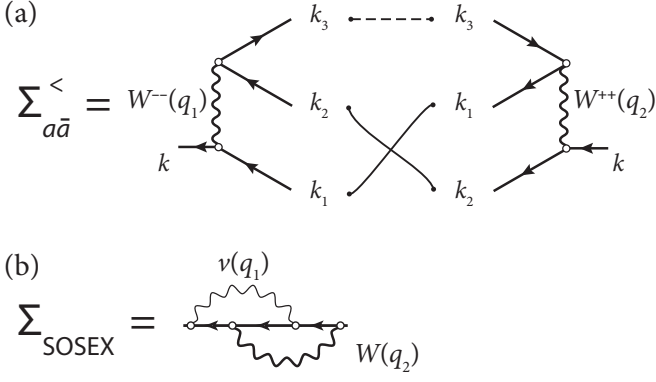


FIG. 4. (a) Gluing two $D^{(a)}$ half-diagrams with one permutation of the two hole lines with momenta $k_1 = k - q_1$ and $k_2 = k - q_2$ and a single hole line $k_3 = k - q_1 - q_2$ (dashed line) yields $\Sigma_{a\bar{a}}^<(k, \omega)$. The unpermuted configuration is not included, therefore the diagram may lead to a negative electron spectral function. Wavy lines denote screened Coulomb interactions. (b) $\Sigma_{\text{SOSEX}}^<$ contains different interaction lines and is thus distinct from $\Sigma_{a\bar{a}}^<$.

have been directed to extend the method towards the valence states [33,34], plasmonic satellites have been observed [8,35] and predicted [36] in a wide range of realistic systems and in the homogeneous electron gas [37,38].

C. $\Sigma_{a\bar{a}}^<$

Finally we consider a rather complicated $\Sigma_{a\bar{a}}^<$ resulting from the $- + +$ partition, Fig. 3(a):

$$\Sigma_{a\bar{a}}^<(1, 2) = -i \sum_{\rho_1, \rho_2, q_1} [D^{(a)} + D^{(b)}]_{\rho_2, \rho_1, q_1}^* (1) \times [D^{(a)} + D^{(b)}]_{\rho_1, \rho_2, q_1}(2). \quad (17)$$

It has a form very similar to Eq. (15), except that the hole indices ρ_1 and ρ_2 are permuted (Fig. 4) leading to the change of sign. The sign of a permutation can be conveniently determined from the number of crossing of fermionic lines connecting the half-diagrams [39]. Neglecting the $D^{(b)}$ diagrams, which only produces a correction to the scattering of a hole state into a 2-holes–1-particle state, and using the explicit form for $D^{(a)}$, Eqs. (3), the self-energy in coordinate representation reads

$$\Sigma_{a\bar{a}}^<(1, 2) = - \iint d(3, 4) W^{--}(1, 3) g^<(1, 4) g^>(4, 3) \times g^<(3, 2) W^{++}(4, 2). \quad (18)$$

Thus, there are two lesser and one greater propagators connecting the $+$ and the $-$ islands. In the momentum-frequency representation they are $g^>(k_3, \omega - \nu_1 - \nu_2) g^<(k_1, \omega - \nu_1) g^<(k_2, \omega - \nu_2)$. They contain δ functions, therefore, the integrals over the internal frequencies $\nu_{1,2}$ are simple. Collecting screened interaction dependent on these frequencies, $W^{--}(q_1, \nu_1) W^{++}(q_2, \nu_2)$, and using the explicit form

$$g^>(k, \omega) = -2\pi i \bar{n}_F(k) \delta[\omega - \epsilon(k)], \quad (19)$$

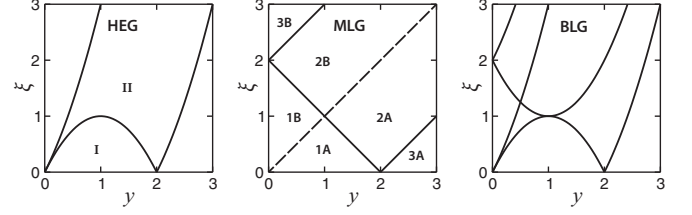


FIG. 5. Domains in the momentum-energy plane in the definitions of the dielectric functions of HEG, MLG, and BLG. Here $y = q/k_F$ and $\xi = \omega/\epsilon_F$.

with $\bar{n}_F(k) = 1 - n_F(k)$, we can write the self-energy explicitly:

$$\begin{aligned} \Sigma_{a\bar{a}}^<(k, \omega) &= 2i\pi \iint d(\Omega_{1,2}) n_F(k_1) n_F(k_2) \bar{n}_F(k_3) \\ &\quad \times W^{--}(q_1, \omega - \epsilon_1) W^{++}(q_2, \omega - \epsilon_2) \\ &\quad \times \delta(\omega - \epsilon_1 - \epsilon_2 + \epsilon_3) \\ &= -2i\pi \iint d(\Omega_{1,2}) n_F(k_1) n_F(k_2) \bar{n}_F(k_3) \\ &\quad \times \text{Re}[W^T(q_1, \omega - \epsilon_1) (W^T(q_2, \omega - \epsilon_2))^*] \\ &\quad \times \delta(\omega - \epsilon_1 - \epsilon_2 + \epsilon_3). \end{aligned} \quad (20)$$

Because of the permutation of ρ_1 and ρ_2 indices, Eq. (17) forms a complete square only in combination with the unpermuted configuration, Eq. (15), and $-i\Sigma_{a\bar{a}}^<$ is not PSD on its own. At least for bare interactions, this can immediately be seen from the equation above. In this case the second-order exchange self-energy Σ_{2x} is obtained.

Because Σ_{2x} is a limit of $\Sigma_{a\bar{a}}$, one might denote the latter as the second-order screened exchange (SOSEX) term. However, this name is already taken as common nomenclature for a different approximation and therefore we will use $\Sigma_{a\bar{a}}$ to contrast it with Σ_{SOSEX} . So, what is the difference between the two? Σ_{SOSEX} has been derived by Freeman [40] and applied to the computation of total energies by Grüneis *et al.* [21] and spectral properties by Ren *et al.* [22]. The starting point is the screened interaction in the RPA form

$$W(1, 2) = v(1, 2) + \int d(3, 4) v(1, 3) \mathcal{P}_0(3, 4) W(4, 2). \quad (22)$$

Σ_{SOSEX} is obtained by inserting the second term in the GW self-energy and interchanging the two electron propagators. As can be seen from Fig. 4(b), one constituent interaction is bare, whereas another one is screened. This is to be contrasted with $\Sigma_{a\bar{a}}$, where both lines are screened. Notice, there is no double counting because they belong to different branches of the Keldysh contour.

IV. SYSTEMS AND REFERENCE RESULTS

In this section we present in a uniform way the four studied systems. We focus on the dielectric function in the momentum-frequency plane, Fig. 5. It is closely connected to the irreducible polarization $\mathcal{P}(q, \omega)$ and to the density-density

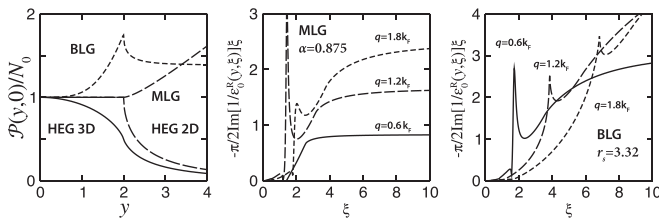


FIG. 6. Static irreducible polarization $\mathcal{P}(q, 0)$ for the four studied systems normalized at the density of states at the Fermi level N_0 (a). N_0 is given by $\rho_\sigma(\epsilon_F)$ for HEG and by $\rho_{\sigma,s}(\epsilon_F)$ for the two graphene systems, $y = q/k_F$ and $\xi = \omega/\epsilon_F$. Integrand of the f -sum rule for MLG (b) and BLG (c) demonstrating the divergence of the f -sum in these systems.

response $\chi(q, \omega)$,

$$\chi(q, \omega) = \mathcal{P}(q, \omega) + \mathcal{P}(q, \omega)v(q)\chi(q, \omega). \quad (23)$$

They determine the microscopic dielectric function and its inverse, respectively,

$$\epsilon(q, \omega) = 1 - gv(q)\mathcal{P}(q, \omega), \quad (24)$$

$$\epsilon(q, \omega)^{-1} = 1 + gv(q)\chi(q, \omega). \quad (25)$$

Here g is the degeneracy factor. For the homogeneous electron gas there is only spin degeneracy, $g = g_s = 2$, whereas for the mono- and bilayer graphene the valley degeneracy additionally appears $g = g_s g_v$. For these systems $g_v = 2$, but it can take larger values for other systems [41,42]. The density of states at the Fermi energy N_0 is a natural unit to measure \mathcal{P} and χ , because the static polarization $\mathcal{P}(q, 0)$ for small values of q is exactly given by this quantity, Fig. 6(a).

The random phase approximation for the inverse dielectric function $\text{Im} \epsilon_0(q, \omega)^{-1}$ is a very important ingredient of the subsequent correlated calculations because this gives [up to the Coulomb prefactor $v(q)$] the spectral function of the screened interaction (Appendix B). A general overview of this quantity is shown in Fig. 7. It is very fortunate that for all four studied systems it can be found in analytic form facilitating numerical calculations. Below, we collect all needed formulas and additionally present the exchange self-energy, which enters Eq. (2).

In the following we express the electron density n , which is the central control parameter, in SI units, in order to make a connection with experiment. All other quantities are expressed in atomic units. Some simplification of formulas is possible to achieve by rescaling momenta and energies by the Fermi momentum k_F and energy ϵ_F , respectively. This will be explicitly indicated.

A. 2D HEG

This is probably the best studied many-body system [24,43]. There is only one relevant parameter—the Wigner-Seitz radius r_s . It is given in terms of electronic density n as follows:

$$a_B r_s = \left(\frac{1}{\pi n} \right)^{1/2}. \quad (26)$$

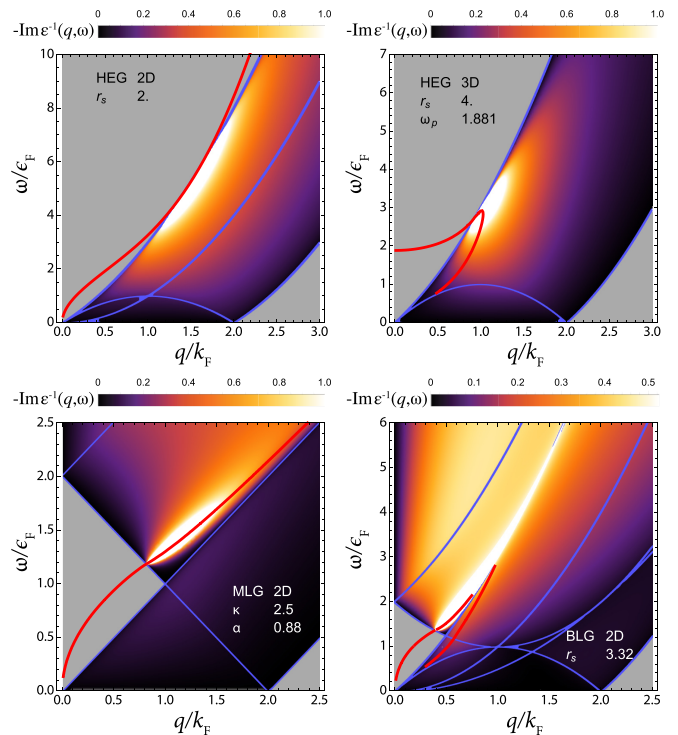


FIG. 7. Imaginary part of the inverse dielectric function for the four studied systems. Red lines indicate the collective plasmonic mode. Blue lines separate different domains in the definition of polarizability such as shown in Fig. 5 and indicate removable singularities.

In the case of systems with an effective electron mass m_0 and a background dielectric constant $\kappa = 4\pi\epsilon\epsilon_0$, one can redefine the Bohr radius as

$$\tilde{a}_B = \frac{\kappa \hbar^2}{m_0 e^2} \quad (27)$$

and still have the same relation between the density and r_s . The Coulomb potential $v(q)$, the Fermi momentum k_F , and the density of states at the Fermi energy $\rho_\sigma(\epsilon_F)$ in atomic units read

$$v(q) = \frac{2\pi}{q}, \quad k_F = \frac{1}{\alpha_2 r_s}, \quad \rho_\sigma(\epsilon_F) = \frac{1}{2\pi}, \quad (28)$$

where we additionally defined the constant

$$\alpha_2 = 1/\sqrt{2}. \quad (29)$$

Introducing scaled variables

$$y = q/k_F, \quad \xi = \omega/\epsilon_F, \quad (30)$$

the dielectric function $\epsilon_0^R(k, \omega) \equiv \epsilon_0^R(y, \xi)$ reads [44]

$$\text{Re} \epsilon_0^R(y, \xi) = 1 + \frac{2\alpha_2 r_s}{y^2} [y + f_r(\xi/y - y) - f_r(\xi/y + y)], \quad (31)$$

$$\text{Im} \epsilon_0^R(y, \xi) = \frac{2\alpha_2 r_s}{y^2} [f_i(\xi/y - y) - f_i(\xi/y + y)], \quad (32)$$

with

$$f_r(z) = \text{sgn}(z)\theta(1/4z^2 - 1)\sqrt{1/4z^2 - 1},$$

$$f_i(z) = \theta(1 - 1/4z^2)\sqrt{1 - 1/4z^2}.$$

For small momentum values, the expression in brackets of Eq. (31) suffers from precision loss. Therefore, in this limit the approximate formula

$$\text{Re } \varepsilon_0^R(y, \xi) = 1 - \frac{\kappa_{\text{TF}} y}{\xi^2}, \quad \kappa_{\text{TF}} = 4\alpha_2 r_s \quad (33)$$

should be used entailing the small-momenta plasmon dispersion $\Omega(y) \approx \sqrt{y\kappa_{\text{TF}}}$. It can also be found analytically (see Eq. 5.54 of Ref. [45]):

$$\Omega(y) = \frac{\sqrt{y}(2y + \kappa_{\text{TF}})\sqrt{y^4 + y^3\kappa_{\text{TF}} + \kappa_{\text{TF}}^2}}{\kappa_{\text{TF}}\sqrt{y + \kappa_{\text{TF}}}}, \quad (34)$$

where κ_{TF} is the Thomas-Fermi screening wave vector in 2D. The critical wave vector does not have a nice analytical expression. However, one can show that $k_c \sim \sqrt{\kappa_{\text{TF}}}$. Notice that even though $\Omega(y) > y(y + 2)$ for $y > k_c$ there is no plasmon above the critical vector because in reality the plasmon becomes damped by entering the continuum, where the above solution is not valid.

The f -sum rule reads in rescaled units

$$-\frac{2}{\pi} \int_0^\infty d\xi \xi \text{Im} \left[\frac{1}{\varepsilon^R(y, \xi)} \right] = \alpha_2 r_s^3 y. \quad (35)$$

The exchange part of the electron self-energy,

$$\Sigma_x(k) = - \int_{|q| < k_F} \frac{d^2 q}{(2\pi)^2} \frac{2\pi}{\kappa |\mathbf{k} - \mathbf{q}|}, \quad (36)$$

can be expressed [45] in terms of the *complete elliptic integrals* (see Sec. 8.112 in Ref. [46]):

$$\bar{\Sigma}_x(y) = -\frac{2}{\pi} \alpha_2 r_s f_{2D}(y), \quad \bar{\Sigma}_x = \Sigma_x / \epsilon_F, \quad (37)$$

$$f_{2D}(y) = \begin{cases} E(y), & y \leq 1, \\ y[E(\frac{1}{y}) - (1 - \frac{1}{y^2})K(\frac{1}{y})], & y > 1. \end{cases} \quad (38)$$

B. 3D HEG

This system also depends on a single parameter—the Wigner-Seitz radius

$$a_{B r_s} = \left(\frac{3}{4\pi n} \right)^{1/3}. \quad (39)$$

It has also been broadly studied [23]. The Coulomb potential $v(q)$, the Fermi momentum k_F , and the density of states at the Fermi energy $\rho_\sigma(\epsilon_F)$ read in atomic units

$$v(q) = \frac{4\pi}{q^2}, \quad k_F = \frac{1}{\alpha_3 r_s}, \quad \rho_\sigma(\epsilon_F) = \frac{1}{2\pi^2 \alpha_3 r_s}, \quad (40)$$

where the relevant constant is defined as

$$\alpha_3 = \left(\frac{4}{9\pi} \right)^{1/3}. \quad (41)$$

The dielectric function is (the Lindhard result)

$$\text{Re } \varepsilon_0^R(y, \xi) = 1 + \frac{\alpha_3 r_s}{\pi y^3} \left[2y + f_r \left(\frac{\xi}{y} - y \right) - f_r \left(\frac{\xi}{y} + y \right) \right], \quad (42)$$

$$\text{Im } \varepsilon_0^R(y, \xi) = \frac{\alpha_3 r_s}{y^3} \left[f_i \left(\frac{\xi}{y} - y \right) - f_i \left(\frac{\xi}{y} + y \right) \right], \quad (43)$$

with

$$f_r(z) = \left(1 - \frac{1}{4}z^2 \right) \log[(z + 2)/(z - 2)],$$

$$f_i(z) = \theta \left(\frac{1}{4}z^2 - 1 \right) \left(1 - \frac{1}{4}z^2 \right).$$

Notice a strong resemblance between the dielectric function in 2D and 3D. This is due to the fact that the upper and lower continuum frequencies are the relevant parameters in both cases (Fig. 5). The shape of the continuum is more complicated for MLG and BLG. However, we will see below that they likewise enter expressions for $\varepsilon_0^R(y, \xi)$.

The f -sum rule is particularly simple in 3D systems. This is due to the form of the Coulomb interaction proportional to q^{-2} (40). Rescaling the frequency and momentum in the usual way (30) we get

$$-\frac{2}{\pi} \int_0^\infty d\xi \xi \text{Im} \left[\frac{1}{\varepsilon^R(y, \xi)} \right] = \omega_p^2, \quad (44)$$

with the classical plasmon frequency (ϵ_F units)

$$\omega_p = 4\sqrt{\frac{\alpha_3 r_s}{3\pi}}. \quad (45)$$

The exchange part of the electron self-energy reads

$$\Sigma_x(k) = - \int_{|q| < k_F} \frac{d^3 q}{(2\pi)^3} \frac{4\pi}{|\mathbf{k} - \mathbf{q}|^2}. \quad (46)$$

Analytical expressions are well-known [45]

$$\bar{\Sigma}_x(y) = -\frac{4}{\pi} \alpha_3 r_s f_{3D}(y), \quad \bar{\Sigma}_x = \Sigma_x / \epsilon_F, \quad (47)$$

$$f_{3D}(y) = \frac{1}{2} + \frac{1 - y^2}{4y} \log \left| \frac{1 + y}{1 - y} \right|. \quad (48)$$

C. 2D MLG

In the model approach to graphene, electronic states of the π bands near a K point of the Brillouin zone are described by the $\mathbf{k} \cdot \mathbf{p}$ equation $\hat{\mathcal{H}}_0 \mathbf{F}(\mathbf{r}) = \epsilon \mathbf{F}(\mathbf{r})$ [41,47], where the Hamiltonian reads

$$\hat{\mathcal{H}}_0 = v_F \begin{pmatrix} 0 & \hat{p}_x - i\hat{p}_y \\ \hat{p}_x + i\hat{p}_y & 0 \end{pmatrix} = v_F (\sigma_x \hat{p}_x + \sigma_y \hat{p}_y), \quad (49)$$

with $\hat{\mathbf{p}} = (\hat{p}_x, \hat{p}_y)$ being the momentum operator and v_F the Fermi velocity (which can be expressed in terms of the hopping integral and the lattice constant [48], the typically adopted value is 10^6 m/s = $1/2.188$ a.u.). The wave function is then

$$\mathbf{F}_{s,\mathbf{k}}(\mathbf{r}) = |s, \mathbf{k}\rangle \frac{1}{L} e^{i\mathbf{k} \cdot \mathbf{r}}, \quad |s, \mathbf{k}\rangle = \frac{1}{\sqrt{2}} \begin{pmatrix} e^{-i\theta_k} \\ s \end{pmatrix}, \quad (50)$$

where L^2 is the area of the system, and $k_x = k \cos \theta_k$, $k_y = k \sin \theta_k$, $k = |\mathbf{k}|$. The corresponding energy dispersion reads

$$\epsilon(k) = s v_F k, \quad (51)$$

which is different from previous cases in two important ways: (i) the well-known linear momentum dependence and (ii) the presence of two bands indicated by the band index $s = \pm 1$ and, as a consequence, the presence of additional matrix

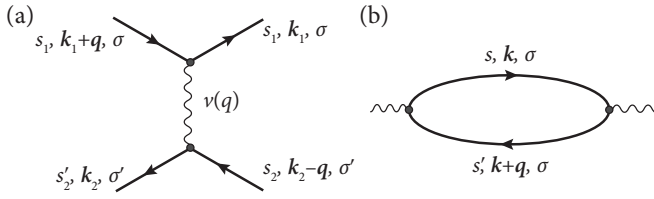


FIG. 8. Diagrammatic representation of (a) the Coulomb interaction (52) and (b) the polarization bubble in MLG. The latter illustrates the appearance of the spin g_s and band g_v degeneracy prefactors in the dielectric function, Eqs. (56) and (58). The overlap matrix elements (62) are represented by shaded vertices.

elements in the Coulomb operator (Fig. 8)

$$\hat{V} = \frac{1}{2L^2} \sum_{\mathbf{q}, \mathbf{k}_1, \mathbf{k}_2} \sum_{s_1, s_2, s'_1, s'_2} \langle s'_1, \mathbf{k}_1 + \mathbf{q} | s_1, \mathbf{k}_1 \rangle \langle s_2, \mathbf{k}_2 - \mathbf{q} | s'_2, \mathbf{k}_2 \rangle \times \sum_{\sigma, \sigma'} \frac{2\pi}{\kappa q} \hat{c}_{s'_1, \mathbf{k}_1 + \mathbf{q}, \sigma}^\dagger \hat{c}_{s_2, \mathbf{k}_2 - \mathbf{q}, \sigma'}^\dagger \hat{c}_{s'_2, \mathbf{k}_2, \sigma'} \hat{c}_{s_1, \mathbf{k}_1, \sigma}. \quad (52)$$

Thus, basis functions are labeled by the momentum \mathbf{k} , band index s , and spin σ . In view of the dispersion (51), the noninteracting GF is diagonal in s and σ . We are interested in the electron self-energy diagonal in the band indices. Furthermore, the calculations are typically performed at finite doping (extrinsic graphene) and with a dielectric function modified by the presence of the substrate. We will focus on the SiO_2 substrate $\kappa = (1 + \epsilon_{\text{SiO}_2})/2 = 2.45$, consider the case of the *electron doping*, i.e., that the Fermi level is above the Dirac point, and follow the notations from the previous sections that

$$\kappa = 4\pi\epsilon\epsilon_0, \quad (53)$$

with ϵ_0 being the vacuum electric permittivity. The Fermi momentum and energy depend on the square root of the electron density

$$k_F = a_B \sqrt{\frac{4\pi n}{g}} = \frac{1}{\langle r \rangle}, \quad \epsilon_F = v_F k_F, \quad (54)$$

$g = g_s g_v$ where $g_s = 2$ is the spin and $g_v = 2$ is the valley degeneracy, respectively. $\langle r \rangle$ is the averaged interelectron distance.

The parameter characterizing the level of correlations in the system is given by the ratio of the Coulomb E_C and the kinetic E_K energies, as is therefore the counterpart of r_s for the homogeneous electron gas

$$\alpha = \frac{E_C}{E_K} = \frac{1}{\kappa} \frac{1}{\langle r \rangle} \frac{1}{v_F k_F} = \frac{1}{\kappa v_F} \simeq \frac{2.188}{\kappa}, \quad (55)$$

for instance, $\alpha = 2.188$ for MLG in vacuum and $\alpha = 0.875$ for the SiO_2 substrate. The dielectric function has been computed by Hwang and Das Sarma [49] and by Wunsch *et al.* [50]. We will use the latter form:

$$\text{Re } \epsilon_0^R(y, \xi) = 1 + \frac{g\alpha}{y} + g\alpha f(y, \xi) G_r(y, \xi), \quad (56)$$

$$\text{Im } \epsilon_0^R(y, \xi) = g\alpha f(y, \xi) G_i(y, \xi), \quad (57)$$

$$f(y, \xi) = \frac{1}{8} \frac{y}{\sqrt{|\xi^2 - y^2|}}, \quad (58)$$

The functions G_r and G_i are defined in Appendix C. The density of states at the Fermi level reads

$$\rho_{\sigma, s} = (2\pi v_F)^{-1}. \quad (59)$$

The static polarizability normalized at this number is plotted in Fig. 6(a). Due to the presence of an infinite sea of electrons below the Dirac point, the f -sum rule diverges as demonstrated by Hwang, Throckmorton, and Das Sarma [51]. The integrand of the f -sum is illustrated in Fig. 6(b).

Due to this fact, a momentum cut-off k_c needs to be introduced for the momentum integrals. In a realistic system this is not a problem because of the bands flattening due to lattice effects [52]. For the idealistic model that we consider here, k_c is an explicit parameter of the theory. We adopt

$$k_c = y_c k_F = 10k_F. \quad (60)$$

The exchange self-energy can be written in the form

$$\Sigma_{x, s}(k) = - \sum_{s' = \pm 1} \int \frac{d^2 q}{(2\pi)^2} n_{F, s'}(|\mathbf{k} - \mathbf{q}|) \frac{2\pi}{\kappa q} F_{s, s'}(\mathbf{k}, \mathbf{k} - \mathbf{q}). \quad (61)$$

In this equation, $F_{s_1, s_2}(\mathbf{k}_1, \mathbf{k}_2)$ takes into account the probability for an electron with momentum \mathbf{k}_1 in the band s_1 to scatter into the state with momentum \mathbf{k}_2 in the band s_2 . It depends on the relative angle θ_{12} between the two momenta,

$$\langle s_2, \mathbf{k}_2 | s_1, \mathbf{k}_1 \rangle = \frac{1}{2} (1 + s_1 s_2 e^{i\theta_{12}}), \quad (62)$$

$$F_{s_1, s_2}(\mathbf{k}_1, \mathbf{k}_2) = |\langle s_2, \mathbf{k}_2 | s_1, \mathbf{k}_1 \rangle|^2 = \frac{1}{2} (1 + s_1 s_2 \cos \theta_{12}). \quad (63)$$

Using the Fermi energy and momentum units, dividing into intrinsic (present in pristine graphene) and extrinsic (due to carriers injection by doping or gating) contributions, shifting by the constant so that the self-energy is zero at the Dirac point [$\Sigma_{x, \pm 1}(0) = 0$] we obtain for Eq. (61)

$$\bar{\Sigma}_{x, s}(y) = \bar{\Sigma}_{x, s}^{\text{int}}(y) + \bar{\Sigma}_{x, s}^{\text{ext}}(y) + \frac{\alpha}{2} (1 + y_c), \quad (64)$$

with

$$\bar{\Sigma}_{x, s}^{\text{int}}(y) = -\frac{\alpha y_c}{\pi} \left[\frac{\pi}{2} - s g \left(\frac{y}{y_c} \right) \right], \quad (65)$$

$$\bar{\Sigma}_{x, s}^{\text{ext}}(y) = -\frac{\alpha}{\pi} \left[f_{2D}(y) + sh(y) \right]. \quad (66)$$

The function $f_{2D}(y)$ has already been defined for the 2D HEG (38). The former intrinsic part results from the integration over the $s' = -1$ band from zero to the momentum cut-off $k_c = y_c k_F$. Functions $h(y)$ and $g(y)$ have a representation (correcting $g(y)$ in the original derivation by Hwang, Hu, and Das Sarma [53]):

$$h(y) = y \begin{cases} \frac{\pi}{4} \log \frac{4}{y e^{1/2}} - \int_0^y \frac{dx}{x^3} [K(x) - E(x) - \frac{\pi x^2}{4}] & y \leq 1, \\ \int_0^{1/y} dx [K(x) - E(x)] & y > 1; \end{cases} \quad (67)$$

$$g(x) = \frac{1}{4} \int_0^1 dy \int_0^{2\pi} d\theta \frac{x - y \cos \theta}{\sqrt{x^2 + y^2 - 2xy \cos \theta}}$$

$$= \frac{\pi}{2} \operatorname{Re} \left\{ {}_3F_2 \left(-\frac{1}{2}, \frac{1}{2}, \frac{1}{2}; 1, \frac{3}{2}; \frac{1}{x^2} \right) \right\}. \quad (68)$$

D. 2D BLG

Consider now two parabolic energy bands

$$\epsilon(k) = sk^2/(2m_0). \quad (69)$$

Unlike MLG, the dispersion is an idealization of several materials with different number of valleys g_v and with large flexibility in the properties control with the help of doping and the background dielectric constant. Here we focus on the $g_v = 2$ case pertinent to the bilayer graphene (a minimal two-band model for the Bernal AB stacking [28]). We have the following relations determining the Fermi energy and momentum, and the Wigner-Seitz radius [54]:

$$\frac{k_F}{a_B} = \sqrt{\frac{4\pi n}{g_s g_v}}, \quad \epsilon_F = \frac{k_F^2}{2m_0}, \quad r_s = \frac{gm_0}{\kappa k_F}, \quad \rho_{\sigma,s}(\epsilon_F) = \frac{m_0}{2\pi}. \quad (70)$$

One may also define the Wigner-Seitz radius as the ratio of two energies

$$\tilde{r}_s = \frac{E_C}{E_K} = \frac{1}{\kappa \langle r \rangle} \frac{2m_0}{k_F^2} = \frac{m_0}{\kappa} \frac{g_s g_v a_B}{(4\pi n)^{1/2}}, \quad a_B \langle r \rangle = \left(\frac{1}{\pi n} \right)^{1/2}.$$

Sensarma, Hwang, and Das Sarma [54] derived the polarizability of this system separating the intra(inter)-band contributions $\Pi = \Pi_1 + \Pi_2$. The former originates from the intraband ($s = s'$) and the latter from interband ($s = -s'$) transitions, Fig. 8(b),

$$\Pi_1(y, \xi) = \frac{1}{\pi} \int_0^1 dx \int_{-\pi}^{\pi} d\phi \frac{x}{\xi + i\eta - 2xy \cos(\phi) - y^2}$$

$$\times \left[1 - \frac{y^2 \sin^2(\phi)}{x^2 + 2xy \cos(\phi) + y^2} \right], \quad (71)$$

$$\Pi_2(y, \xi)$$

$$= -\frac{1}{\pi} \int_0^1 dx \int_{-\pi}^{\pi} d\phi \frac{x}{\xi + i\eta + 2x^2 + 2xy \cos(\phi) + y^2}$$

$$\times \frac{y^2 \sin^2(\phi)}{x^2 + 2xy \cos(\phi) + y^2}. \quad (72)$$

The retarded polarizability is given by

$$\operatorname{Re} \mathcal{P}(y, \xi) = \operatorname{Re} \Pi(y, \xi) + \operatorname{Re} \Pi(y, -\xi), \quad (73)$$

$$\operatorname{Im} \mathcal{P}(y, \xi) = \operatorname{Im} \Pi(y, \xi) - \operatorname{Im} \Pi(y, -\xi). \quad (74)$$

Π_1 is fully defined in the paper [54]. There are, however, some misprints in the extrinsic part that are corrected here in Appendix D. The dielectric function is given by

$$\epsilon_0^R(y, \xi) = 1 - \frac{r_s}{y} \mathcal{P}(y, \xi). \quad (75)$$

The static polarizability was derived by Hwang and Das Sarma [55] and is plotted here for comparison with other

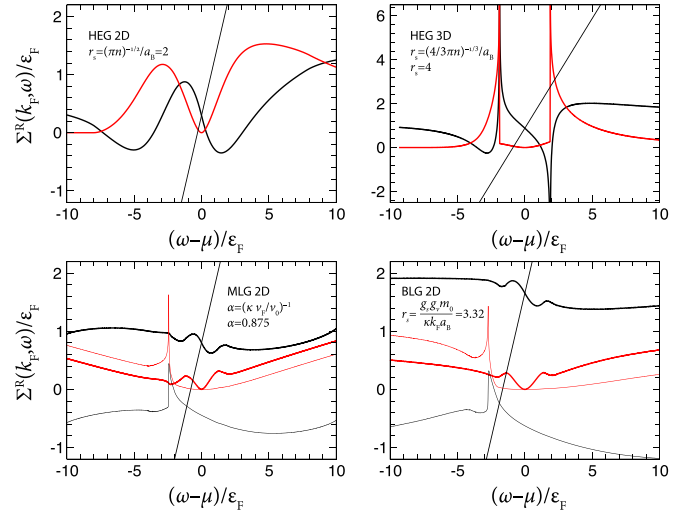


FIG. 9. Solution of the Dyson equation for the Fermi level $k = k_F$. Intersection of straight line $y = \omega - \epsilon_F - \Delta\mu$ and $y = \operatorname{Re} \Sigma^R(k_F, \omega)$ (thick black curve) yields the real part of the quasi-particle energy. The chemical potential shift $\Delta\mu$ is selected (see Appendix E) as to have the imaginary part zero in accordance with the Fermi liquid assumption. Red curves stand for $\frac{1}{2} \Gamma(k_F, \omega) = -\operatorname{Im} \Sigma^R(k_F, \omega)$. In the case of MLG and BLG thick/thin curves correspond to $\Sigma_{s=\pm 1}^R(k_F, \omega)$.

systems in Fig. 6(a). The f -sum rule diverges for this system for the same reasons as for MLG. The integrand of the f -sum is illustrated in Fig. 6(c). The exchange self-energy is the same as for MLG (66).

E. G_0W_0 calculations

Before presenting calculations with vertex functions, we review the electron self-energy in the simplest G_0W_0 approximation, Eq. (14). The self-energy is depicted in Fig. 9, the respective electron spectral function

$$A(k, \omega) = -2 \operatorname{Im} G^R(k, \omega) \quad (76)$$

is shown in Fig. 10.

1. HEG

The homogeneous electron gas systems have a long history of studies: Lundqvist [23], Hedin [1], and self-consistent GW calculations by von Barth and Holm [7,56] in 3D and Giuliani and Quinn [57], Santoro and Giuliani [24], Zhang and Das Sarma [58], and Lischner *et al.* [59] in 2D. Because of the way the 2D HEG is engineered (its properties can be tuned by doping and the electron concentration), it is easy to go to the strongly correlated regime and still have a homogeneous system. Therefore, correlations beyond G_0W_0 have been included almost from the beginning. Thus, Santoro and Giuliani included the many-body local fields G_{\pm} in the calculation of screening and employed the plasmon-pole approximation. This yields a self-energy resembling the 3D case and results in a more pronounced plasmon peak as compared to the G_0W_0 calculations.

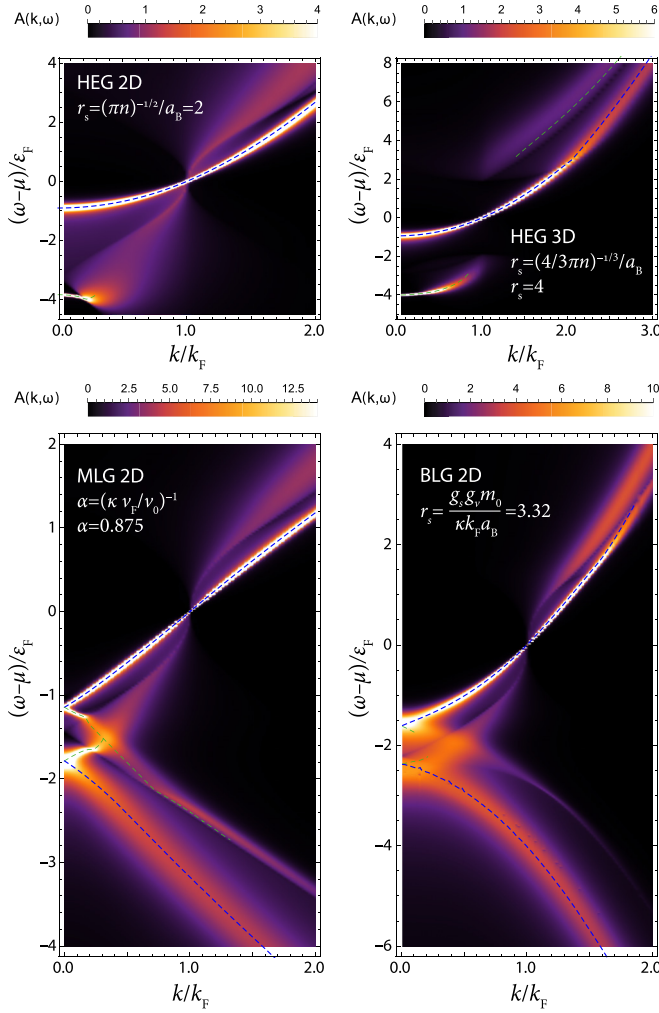


FIG. 10. The electron spectral function from the solution of the Dyson equation with self-energy in G_0W_0 approximation. For MLG and BLG, the spectral function is a matrix in the band indices, the trace of it is shown here.

2. Graphene

There are two peculiarities in the case of MLG and BLG systems. (i) The electron dispersion and self-energies additionally carry the valley index s resulting in the following modification of Eq. (14):

$$\Sigma_{GW,s}^<(k, \omega) = 2i\pi \sum_{s'=\pm 1} \int_0^{q_1 \leq k_c} \frac{d^2 q_1}{(2\pi)^2} \int_0^\infty dv_1 F_{s,s'}(\mathbf{k}; \mathbf{k}_1) \times n_{F,s'}(k_1) C(q_1, v_1) \delta(\omega + v_1 - \epsilon_1), \quad (77)$$

where the scattering matrix element $F_{s,s'}$ is given by Eq. (63). (ii) Due to the presence of an infinite electron sea below the Dirac point the diverging momentum integrals need to be regularized with the help of cut-off (60). One can also introduce a frequency cutoff without compromising the accuracy.

Hwang and Das Sarma [25] and Polini *et al.* [26] performed calculations for MLG, and more extensive investigations for a range of momenta are in Refs. [60–63]. Respective calculations for BLG have been performed by Sensarma, Hwang, and Das Sarma [27] and Sabashvili *et al.* [64].

V. $\Sigma_{a\bar{a}}$: SCATTERING ACCOMPANIED BY THE GENERATION OF A ph PAIR WITH EXCHANGE

$\Sigma_{a\bar{a}}$ is the main objective of this work. It describes the simplest second-order process in which a particle scatters giving rise to an additional particle-hole pair in the final state, Fig. 4. It is obtained by gluing two half-diagrams $D^{(a)}$ with a permutation, and therefore does not lead to a PSD spectral functions on its own. However, the inclusion of an unpermuted configuration gives rise to Σ_{aa} restoring the PSD property. In this work $\Sigma_{a\bar{a}}$ is computed according to Eq. (20), which needs some modifications in the case of graphene in order to account for the band indices. After discussing this technical point in Sec. V A, we consider the influence of screening on $\Sigma_{a\bar{a}}$ in Sec. V B, the cancellations between Σ_{aa} and $\Sigma_{a\bar{a}}$ in the asymptotic regime in Sec. V C, and finally focus on the resulting quasiparticle properties in Sec. V D.

A. Computation for MLG and BLG systems

In the case of graphene, Eq. (20) additionally gets a sum over three internal band indices and an additional factor, which is a product of the four wave-function overlaps,

$$F_{s_0, s_1, s_2, s_3}(\mathbf{k}_0; \mathbf{k}_1, \mathbf{k}_2, \mathbf{k}_3) = \langle s_0, \mathbf{k}_0 | s_1, \mathbf{k}_1 \rangle \langle s_1, \mathbf{k}_1 | s_3, \mathbf{k}_3 \rangle \times \langle s_3, \mathbf{k}_3 | s_2, \mathbf{k}_2 \rangle \langle s_2, \mathbf{k}_2 | s_0, \mathbf{k}_0 \rangle = \frac{1}{8} \left\{ 1 + \sum_{i < j} s_i s_j \cos \theta_{ij} + s_0 s_1 s_2 s_3 \cos(\theta_{01} + \theta_{32}) \right\}, \quad (78)$$

where θ_{ij} is the angle between the respective momenta. The second-order exchange then takes a form

$$\Sigma_{2x,s}^<(k, \omega) = -2i\pi \sum_{s_1, s_2, s_3} \iint d(\Omega_{1,2}) F_{s, s_1, s_2, s_3}(\mathbf{k}; \mathbf{k}_1, \mathbf{k}_2, \mathbf{k}_3) \times v(q_1) v(q_2) n_F(k_1) n_F(k_2) \bar{n}_F(k_3) \times \delta(\omega - \epsilon_1 - \epsilon_2 + \epsilon_3), \quad (79)$$

where the momenta are defined by Eq. (10) and depicted in Fig. 3(a). It should be noted that our original PSD construction was formulated for the systems free of the ultraviolet divergences. Here it is applied to graphene, for which the momentum integrals are regularized with the wave-vector cutoff k_c with the justification that the regularization can be implemented on the level of the Hamiltonian.

B. Σ_{2x} results for 3D HEG

The corresponding imaginary part is plotted in Fig. 11. The Hilbert transform (Appendix A) yields the real part. In the inset we see a very good agreement of our numerical result with the analytical expression

$$\epsilon_{2x} = \text{Re } \Sigma_{2x}(k_F, \mu)/\epsilon_F = \frac{\alpha^2 r_s^2}{2\pi^2} \left(\frac{2\pi^2}{3} \ln(2) - 3\zeta(3) \right),$$

that is known due to the calculations of Glasser and Lamb [65] and Ziesche [16] or from the second-order correction to the total energy computed by Onsager *et al.* [66]. According to the Hugenholtz-van Hove-Luttinger-Ward theorem they are

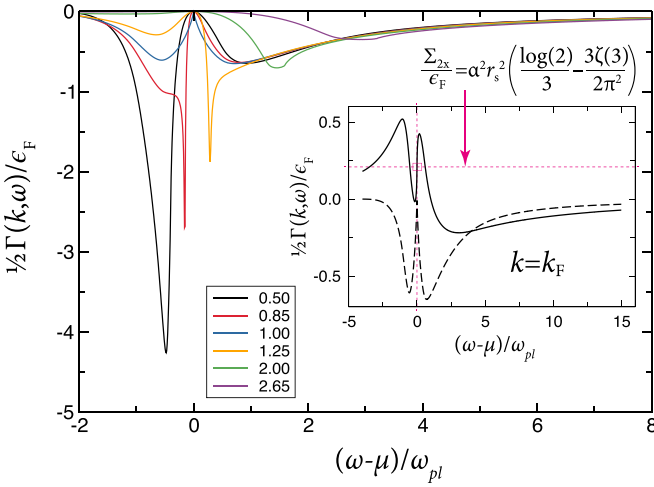


FIG. 11. Σ_{2x} at different momentum values. The inset shows the real self-energy part (solid line) obtained from the Hilbert transform of $\Gamma_{aa}(k_F, \omega)$. Its on-shell value [$\epsilon_{2x}(k_F, \mu) = 0.204976$] has only 2.4% deviation from the indicated analytic result (0.210073).

equal. Despite claims [67], it seems impossible to get the respective expression in analytic form for the 2D HEG [68].

Going away from $k = k_F$, the self-energy first develops an additional sharp peak in the vicinity of $\omega = \mu$ as seen for $k = 0.85k_F, 1.25k_F$, which eventually becomes smeared out, Fig. 12. This is a rather disturbing fact because large negative values need to be compensated by Σ_{aa} , which does not have any singularities in this energy range. Thus, a better understanding of the origin of this peak is needed.

In Fig. 13 we replot $i\Sigma_{aa}^<$ computed with a bare Coulomb interaction for different momentum values paying attention to the kinematic aspects. In particular, we are interested in the

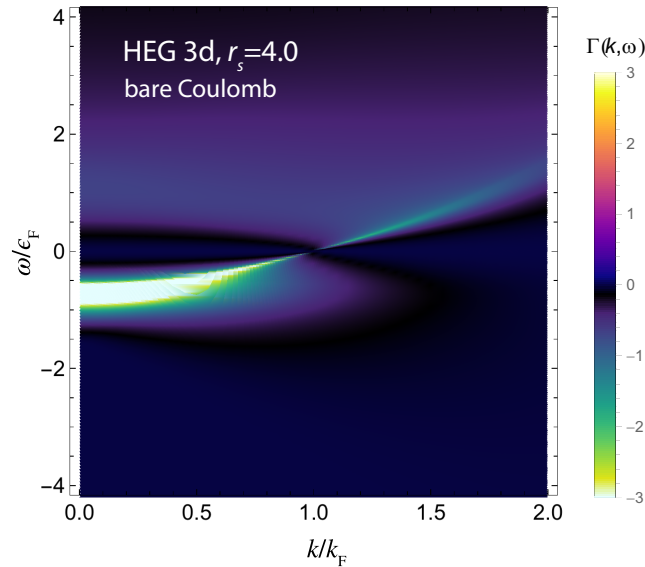


FIG. 12. The momentum- and energy-resolved scattering rate computed with the bare Coulomb interaction for $r_s = 4$. It is negative and possesses a strong peak due to the small-momentum forward scattering. Screening greatly reduces its magnitude, whereas Σ_{aa} compensates for the negative values.

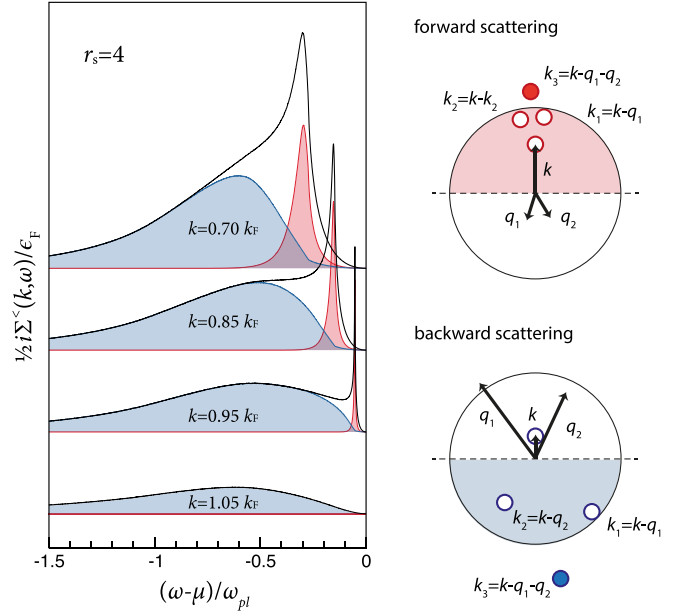


FIG. 13. Σ_{2x} at different momentum values resolved with respect to forward (red) and backward (blue) scattering mechanisms. For a hole in the center of the Fermi sphere $k \ll k_F$, backward scattering dominates, while for a hole close to the Fermi surface $k \approx k_F$, forward scattering with a small momentum transfer gives rise to a sharp peak.

distribution of momenta carried by the two interaction lines $\mathbf{q}_{1,2}$ and, correspondingly, in the configuration of the final state formed by two holes with momentum $\mathbf{k}_{1,2} = \mathbf{k} - \mathbf{q}_{1,2}$ and a particle $\mathbf{k}_3 = \mathbf{k} - \mathbf{q}_1 - \mathbf{q}_2$, Fig. 4. It is, of course, difficult to depict all the multitude of possibilities taking place in our Monte Carlo simulations. However, a useful classification of the involved physical processes can be found: we distinguish the forward and the backward scatterings scenarios. The former is defined as a process in which \mathbf{q}_1 and \mathbf{q}_2 are *antiparallel* to the initial hole momentum, i. e., the scalar products $(\mathbf{k}, \mathbf{q}_1)$ and $(\mathbf{k}, \mathbf{q}_2)$ are negative. In this case the initial hole state with momentum \mathbf{k} gets transformed into two-hole states with momenta in the same Fermi hemisphere (red). For the backward scattering both of these products are positive and, correspondingly, the final hole states are in the opposite hemisphere. From the scheme depicted in Fig. 13 it becomes evident that there is a very limited phase space for the forward mechanism if the initial hole is in the vicinity of Fermi sphere $k \rightarrow k_F$. In order to guarantee that $k_{1,2} \leq k_F$ and $k_3 > k_F$ the interaction momenta $\mathbf{q}_{1,2}$ must be small and almost collinear with \mathbf{k} . As a result we have a “hot spot” in the momentum space where all the permitted configurations contribute in a very narrow energy interval giving rise to a pronounced forward peak. If the initial state is closer to the center of the Fermi sphere, there are less restrictions on the possible scattering angles. Therefore, the forward peak broadens, and for larger energy transfers the backward scattering dominates. It is interesting to notice that the mixed mechanism, i.e., where one hole is in the forward and another in the backward direction, has a rather small contribution and takes place at intermediate energies.

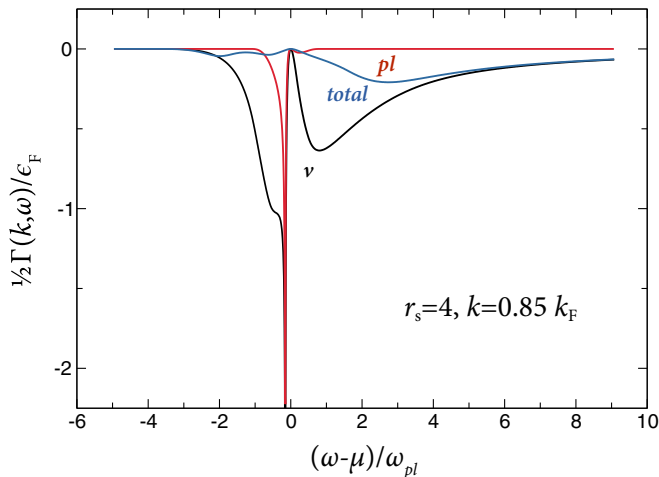


FIG. 14. $\Sigma_{a\bar{a}}$ computed with full RPA screenings W_0 (total), plasmon pole approximation for W_0 (pl), and bare Coulomb interaction (v). Screening, which is operative at small momentum transfers, is responsible for the cancellation of singularity.

From our analysis it follows that small momentum transfers $q_{1,2}$ are important for the appearance of the forward peak. In this regime the Coulomb interaction is screened by plasmons suggesting that the inclusion of screening may reduce the peak. Therefore, we performed three calculations for $k = 0.85k_F$ with (i) bare Coulomb lines, (ii) with only plasmon screening, and (iii) using the fully screened RPA W_0 . They indeed demonstrate that the plasmonic contribution to $\Sigma_{a\bar{a}}$ is essential for compensating the singularity in the bare Coulomb term (Fig. 14). Notice that they both appear with the same sign because the interactions enter quadratically in the expression for $\Sigma_{a\bar{a}}$. As a result, a smooth frequency dependence free of any singularities is obtained for the sum of all contributions.

C. Cancellations between $\Sigma_{aa}^<$ and $\Sigma_{a\bar{a}}^<$ in the asymptotic regime

The asymptotic regime $\omega \rightarrow \pm\infty$ is important because there Σ_{aa} approaches zero, and a failure of the PSD construction would be evident. It is convenient to perform derivations using scaled variables $\mathbf{x}_i = \mathbf{k}_i/k_F$, $\mathbf{y}_i = \mathbf{q}_i/k_F$, $\zeta = \omega/\epsilon_F$.

1. 3D HEG

The G_0W_0 self-energy scales in the high-frequency limit [29] as

$$\frac{i}{2}\overline{\Sigma}_{aa}^>(x, \zeta) \equiv \frac{i}{2}\Sigma_{aa}^>(k/k_F, \omega/\epsilon_F)/\epsilon_F \xrightarrow{\zeta \rightarrow \infty} c_1 \frac{\alpha_3^2 r_s^2}{\zeta^{3/2}}, \quad (80)$$

$$c_1 = \frac{16\sqrt{2}}{3\pi}. \quad (81)$$

Conversely, this determines the short-time behavior of the electron GF. Unexpectedly, Vogt *et al.* [69] have demonstrated that the second-order exchange Σ_{2x} asymptotically scales in the same way, but with an additional $-1/2$ prefactor. This result can be further generalized and derived as follows.

The generalization concerns the fact that in the high frequency limit, the screening is not important and the screened interactions in the expression for $\Sigma_{a\bar{a}}$ can be replaced with the

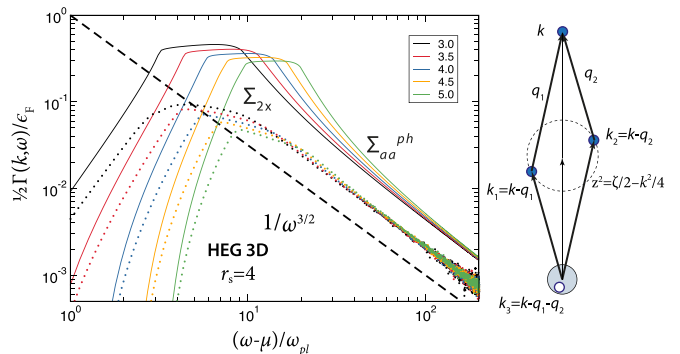


FIG. 15. Asymptotic behavior of $i\Sigma_{aa}^>$ (only p - h excitations) and $-i\Sigma_{2x}^>$ for large momentum values plotted on the logarithmic scale. The latter quantity is negative and therefore is multiplied with -1 . A scheme on the right illustrates momentum configuration of $p \rightarrow p + p + h$ scattering at large energy and momentum transfer, i.e., in the asymptotic regime $\omega \gg k^2/2 \gg \epsilon_F$. In this limit $k_3 \ll k$ and can be integrated over.

bare Coulomb, i.e., $W^{--}(q_1, \omega - \epsilon_1) \rightarrow v(q_1)$, $W^{++}(q_2, \omega - \epsilon_2) \rightarrow v(q_2)$. This means that $\Sigma_{a\bar{a}}$ asymptotically behaves as Σ_{2x} . Using the momenta flow as in Fig. 3(a), the second-order exchange reads

$$\begin{aligned} \frac{i}{2}\overline{\Sigma}_{2x}^>(x, \zeta) &= -\frac{\alpha_3^2 r_s^2}{\pi^3} \iint \frac{d^3\mathbf{y}_1}{y_1^2} \frac{d^3\mathbf{y}_2}{y_2^2} \bar{n}_F(x_1) \bar{n}_F(x_2) n_F(x_3) \\ &\quad \times \delta(\zeta - \epsilon_1 - \epsilon_2 + \epsilon_3). \end{aligned} \quad (82)$$

In the asymptotic case $\zeta \gg x^2/2 \gg 1$ we have $x_3 \ll x_{1,2}$. We change the variables

$$\mathbf{y}_{1,2} = \frac{1}{2}\mathbf{x} \pm \mathbf{z} = \mathbf{x}_{2,1}$$

and integrate over \mathbf{x}_3 within the Fermi sphere (from the scheme in Fig. 15 it is evident that to a good approximation the integrand is independent of x_3) yielding the $4\pi/3$ prefactor to the following remaining integral:

$$\begin{aligned} \frac{i}{2}\overline{\Sigma}_{2x}^>(x, \zeta) &\approx -\frac{4\alpha_3^2 r_s^2}{3\pi^2} \int \frac{d^3\mathbf{z}}{|\frac{1}{2}\mathbf{x} - \mathbf{z}|^2 |\frac{1}{2}\mathbf{x} + \mathbf{z}|^2} \delta\left(\zeta - \frac{1}{2}x^2 - 2z^2\right) \\ &= -\frac{8\alpha_3^2 r_s^2}{3\pi} \frac{\tanh^{-1}\left(\frac{x\sqrt{2\zeta - x^2}}{\zeta}\right)}{\zeta x} \\ &= -\frac{8\sqrt{2}}{3\pi} \alpha_3^2 r_s^2 \zeta^{-3/2} + \mathcal{O}(x^2). \end{aligned} \quad (83)$$

In the last step we exploit the high-frequency assumption $\zeta \gg x^2/2$ and perform a series expansion in x to get the conjectured scaling $i\overline{\Sigma}_{2x}^>(x, \zeta) \xrightarrow{\zeta \rightarrow \infty} c_2 \alpha_3^2 r_s^2 \zeta^{-3/2}$. The scaling is verified numerically in Fig. 15 confirming that the constant c_2 computed from Eq. (83) is momentum independent. It is important, however, that $c_2 = -\frac{1}{2}c_1$ ensuring the PSD property in the high-frequency limit.

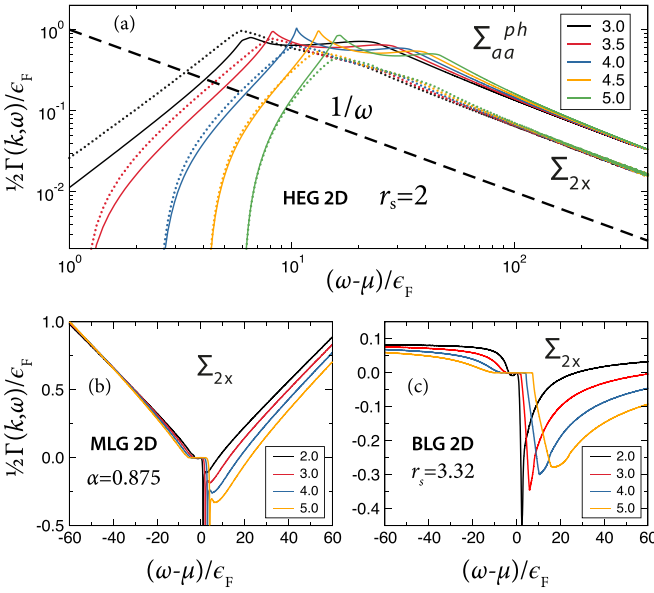


FIG. 16. Top: Asymptotic behavior of the rate functions $i\Sigma_{aa}^>$ (only p - h excitations) and $-i\Sigma_{2x}^>$ for large momentum values plotted on the logarithmic scale for 2D HEG. As in the 3D HEG, they possess the $c_{1,2}/\omega$ scaling, respectively, with $c_2 = -1/2c_1$. (b) and (c) The rate function of the two graphene systems is plotted for different momentum values. There is no universal scaling.

2. 2D HEG

The derivation follows the same line:

$$\begin{aligned} \frac{i}{2}\Sigma_{2x}^>(x, \zeta) &\approx -2 \int \frac{d^2z}{|\frac{1}{2}\mathbf{x} - \mathbf{z}| |\frac{1}{2}\mathbf{x} + \mathbf{z}|} \delta\left(\zeta - \frac{1}{2}x^2 - 2z^2\right) \\ &= -\frac{4}{|\zeta - x^2|} K\left(\frac{x\sqrt{x^2 - 2\zeta}}{\zeta - x^2}\right) \\ &= -\frac{2\pi}{\zeta} + \mathcal{O}(x^2), \end{aligned} \quad (84)$$

where K is a complete elliptic integral. As in the case of the 3D HEG, there is a universal (momentum-independent) asymptotic scaling, see Fig. 16(a), and the ratio of the prefactors is the same. This is yet another exact analytical statement about the second-order self-energy.

3. Graphene systems

The situation is much more complex in the case of graphene, Figs. 16(b) and 16(c). Besides the usual scattering processes considered above, $\Sigma_{a\bar{a}}$ contains processes in which particles change the band, Fig. 17. For instance, for $k > k_F$ our calculations indicate that $\Sigma_{2x}(k, \omega)$ is dominated by the process with $s_3 = -s_1 = -s_2 = 1$ for $\omega < 0$, and with $-s_3 = s_1 = s_2 = 1$ for $\omega > 0$, see Eq. (78). This leads to scattering rates that do not tend to zero as $\omega \rightarrow \pm\infty$. They are cut-off dependent and should be treated as in the case of the first-order exchange.

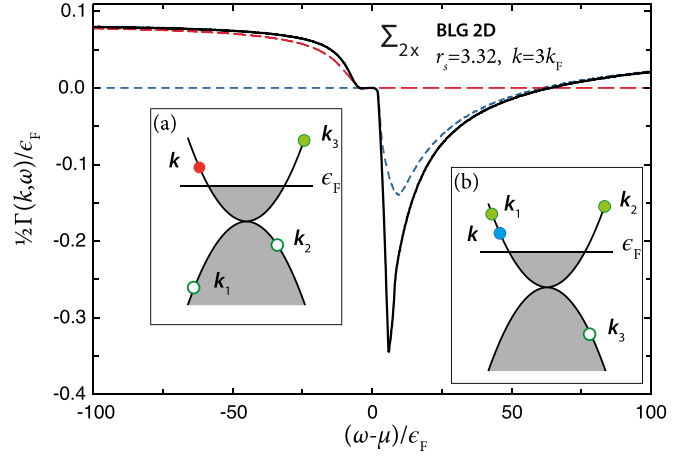


FIG. 17. Second-order exchange in the BLG system for $k = 3k_F$. Besides common scattering channels, the $\omega \rightarrow \infty$ behavior is dominated by processes (blue line) with one hole in the lower band, $s_3 = -1$ (inset b), for $\omega \rightarrow -\infty$ a mechanism with two holes in the lower band $s_1 = s_2 = -1$ is dominating (inset a).

D. Quasiparticle properties

All four considered systems possess very distinct spectral functions. In the vicinity of the quasiparticle peak they can be represented by the Lorentzian form

$$A(k, \omega) = Z_{qp} \frac{1/\tau(k)}{[\omega - \epsilon_{qp}(k)]^2 + 1/[2\tau(k)]^2}, \quad (85)$$

where the peak position $\epsilon_{qp}(k)$, the inverse lifetime $1/\tau(k)$, and the quasiparticle renormalization factor Z_{qp} can be determined by solving the Dyson equation with the given retarded self-energy operator (see Sec. 13.1 in Ref. [30]). In general, one has to take care whether the spectral density can really be written in this form with *finite* Z_{qp} . For instance, this might be not the case in undoped graphene [70,71], or 2D systems with short-range repulsive interactions [72], but *is* the case for the systems considered here. As can be seen from Fig. 18,

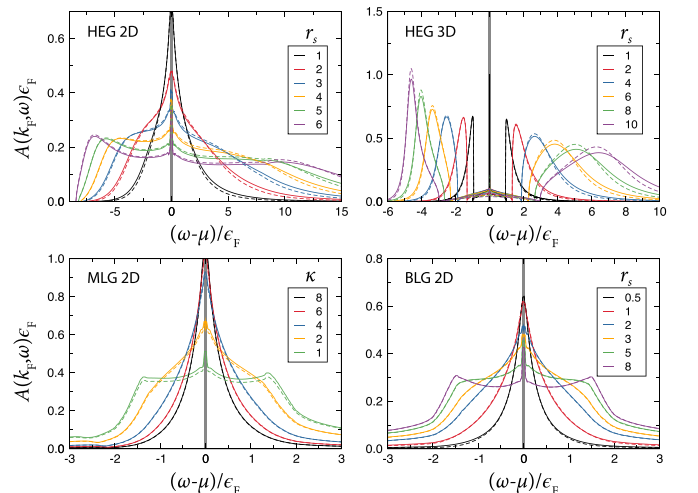


FIG. 18. Electron spectral functions for quasiparticle states at the Fermi surface ($k = k_F$) for different interaction strengths. Dashed lines stand for the G_0W_0 results, full lines—additionally include $\Sigma_{a\bar{a}}$.

the second-order self-energy has a rather small impact on the shape of the quasiparticle peak and its satellites. Therefore, in order to quantify the effect we compute the quasiparticle peak strength:

$$Z_{qp}(k) = \left(1 - \frac{\partial}{\partial \omega} \text{Re} \Sigma^R(k, \omega) \Big|_{\omega=\epsilon_{qp}(k)} \right)^{-1}. \quad (86)$$

We further characterize the quasiparticle dispersion in terms of the effective mass:

$$\frac{1}{m^*} = \frac{1}{k_F} \frac{d\epsilon_{qp}(k)}{dk} \Big|_{k=k_F}, \quad (87)$$

and the Fermi velocity (for MLG)

$$v_F^* = \frac{d\epsilon_{qp}(k)}{dk} \Big|_{k=k_F}. \quad (88)$$

Finally, the inverse quasiparticle lifetime is computed,

$$\tau(k)^{-1} = Z_{qp}(k) \Gamma[k, \epsilon_{qp}(k)], \quad (89)$$

$$\frac{1}{2} \Gamma(k, \omega) = -\text{Im} \Sigma^R(k, \omega). \quad (90)$$

We are mostly interested in the correlated regime $r_s \gg 1$. However, the asymptotic results $r_s \rightarrow 0$ are also shown when available in order to demonstrate that they are valid in a rather very narrow density interval. Our main comparison is with three classes of theories. As benchmarks for the homogeneous electron gas, the quantum Monte Carlo results of Holzmann *et al.* [73] (2D) and [74] (3D) are used. The second class of methods has been advocated by Giuliani and co-workers: Ref. [75] (2D) and Ref. [76] (3D). They improve upon G_0W_0 by using parametrized data from QMC calculations in terms of the charge and the spin static local fields factors $G_+(q)$ and $G_-(q)$, respectively. In their method, the self-energy is in the GW form, however, the screened interaction is replaced by the Kukkonen-Overhauser effective interaction [77]. Furthermore, a diagrammatic approach based on the Bethe-Salpeter equation for the improved screened interaction by Kutepov and Kotliar [78] is also used for comparison. Unfortunately, none of these theories are available for graphene systems.

We start by compiling the data for homogeneous electron gases in 2D and 3D and the bilayer graphene. In these systems r_s is the relevant parameter that can be controlled by doping or other means. In MLG, there is only an indirect possibility to control α by changing the background dielectric constant and κ . This system will be considered later.

1. r_s as a control parameter

In Fig. 19 the quasiparticle renormalization factor $Z_{qp}(k_F)$ as a function of the density parameter r_s is shown. As expected, the agreement between different methods deteriorates with increasing r_s , moreover the quantum Monte Carlo results are not available for BLG. Therefore, it is hard to say with absolute certainty what is the ‘‘right’’ value. On the positive side, we see a very nice convergence of all methods towards the linear asymptote

$$Z_{qp} = 1 - \left(\frac{1}{2} + \frac{1}{\pi} \right) \alpha_2 r_s, \quad 2\text{D}, \quad (91)$$

$$Z_{qp} = 1 - \frac{c}{\pi^2} \alpha_3 r_s, \quad 3\text{D}. \quad (92)$$

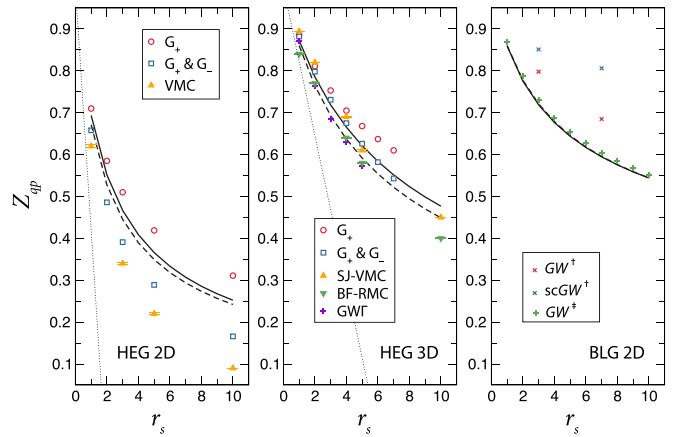


FIG. 19. Quasiparticle renormalization factor for $k = k_F$ and different interaction strengths: $\Sigma_{G_0W_0}$ dashed line, $\Sigma_{G_0W_0} + \Sigma_{aa}$ solid lines. For 2D HEG, the variational Monte Carlo (VMC) results are taken from Ref. [73], and the VMC calculations using Slater-Jastrow (SJ) wave functions and backflow (BF) reptation Monte Carlo (RMC) for 3D HEG from Ref. [74]. $G_+(q)$ and $G_+(q) \& G_-(q)$ denote methods based on the local structure factors from Ref. [75] (2D) and Ref. [76] (3D). $GW\Gamma$ is a scheme D of Ref. [78], it includes the first-order vertex function in the finite temperature formalism. For BLG, † Ref. [64], ‡ Ref. [79].

with $c = -\int_0^{\pi/2} \log(1 - x \cot x) dx \approx 3.353$. The 3D result is by Daniel and Vosko [80], and the 2D asymptote together with temperature corrections is due to Galitski and Das Sarma [81]. For BLG, the effect of Σ_{aa} is negligible, and our calculations accurately reproduce the corrected results of Sensarma *et al.* [79], whereas the one-shot and the self-consistent GW calculations of Sabashvili *et al.* [64] deviate. For the HEG in 2D and 3D, the inclusion of Σ_{aa} slightly increases the value of Z_{qp} . It is interesting to notice that the same trend is observed when the charge local field factor $G_+(q)$ is included. For the 2D HEG, the additional inclusion of both local fields reduces Z_{qp} in agreement with variational MC calculations. At variance, for the 3D HEG the effect of the spin local field is less pronounced [76], and is nearly the same as in our calculations with Σ_{aa} . The effect of the vertex function in Ref. [78] is rather small, therefore, it would be interesting if these calculations could be extended towards larger r_s , where even variational and backflow reptation MC results are in disagreement.

Less accurate are the predictions of different theories for the effective mass, Fig. 20. The situation gets complicated due to different methods of its determination adopted in the literature [58,75]. In order to avoid any ambiguities, the masses in our approach are obtained per definition, that is by solving the Dyson equation for $\epsilon_{qp}(k)$ and using Eq. (87), and *not* by using the self-energy representation

$$\frac{1}{m^*} = \frac{Z_{qp}^{-1}}{1 + \frac{1}{k_F} \frac{d\text{Re}\Sigma^R(k, \epsilon_F)}{dk} \Big|_{k=k_F}}. \quad (93)$$

For weakly interacting systems, $r_s \rightarrow 0$ (high-density limit), we compare with asymptotic expansions. A general form [58] valid for 2D and 3D homogeneous electron gases

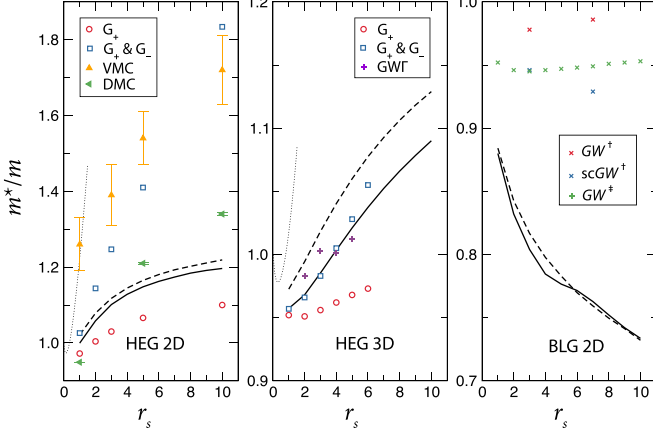


FIG. 20. Effective mass for different interaction strengths: $\Sigma_{G_0W_0}$ dashed line, $\Sigma_{G_0W_0} + \Sigma_{a\bar{a}}$ solid lines. For 2D HEG, the variational Monte Carlo (VMC) results are taken from Ref. [73], and the DMC calculations from Ref. [82]. $G_+(q)$ and $G_-(q)$ and $G_+(q)$ denote methods based on the local structure factors from Ref. [75] (2D) and Ref. [76] (3D). $GW\Gamma$ is a scheme D of Ref. [78], it includes the first-order vertex function in the finite temperature formalism. For BLG, † Ref. [64], ‡ Ref. [79].

reads

$$m^* = 1 + ar_s(b + \log r_s). \quad (94)$$

The coefficients a and b in three dimensions can be inferred from the well-known result of Gell-Mann [83] for the specific heat. The correction in the linear temperature-dependent term due to the electron-electron interaction is entirely attributed to the mass renormalization [84], and therefore

$$m^* = 1 + \frac{1}{2} \frac{\alpha_3 r_s}{\pi} \left(\log \frac{\alpha_3 r_s}{\pi} + 2 \right). \quad (95)$$

In two dimensions, the original derivation is due to Janak [85], whereas the corrected formula² can be found in Saraga and Loss [88]

$$m^* = 1 + \frac{\alpha_2 r_s}{\pi} \left(\log \frac{\alpha_2 r_s}{2} + 2 \right). \quad (96)$$

The asymptotic expressions are derived with the help of additional approximations (e.g., static screening), which quickly invalidates them as r_s increases, see dotted lines in Fig. 20.

Let us now inspect the influence of $\Sigma_{a\bar{a}}$ on the effective mass, which is the difference between the full and the dashed lines. One impressive observation is that for the 3D HEG, our calculations agree again very well with results of Simion and Giuliani [76], where both local field factors are taken into account. The charge local field alone tends to underestimate the effective mass for both systems. A rather poor performance of the Monte Carlo methods is evident for the 2D HEG as well, further calculations of effective masses and extensive comparisons can be found in Drummond and Needs [82].

²There has been some controversies in this derivation. For instance, some mistakes in the original result were pointed out Refs. [86,87], but not explicitly corrected; wrong coefficients a and b can be seen in Refs. [58,81].

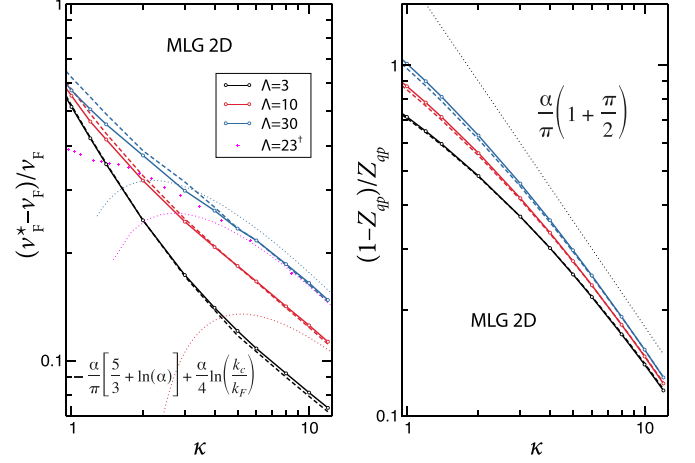


FIG. 21. Renormalized Fermi velocity and the quasiparticle renormalization factor of the monolayer graphene for different values of the momentum cut-off $\Lambda = k_c/k_F$ as a function of dielectric constant. The log-log plots are compared with the scalings from Ref. [90] (dotted lines). † Data from Ref. [63].

However, the difficulties to extract excited state properties from these methods are understandable, and the work of Eich, Holzmann, and Vignale [89] provides some justification.

For BLG, the mass renormalization substantially deviates in comparison with Sensarma *et al.* [79]. This might be due to a different procedure based on Eq. (93) adopted in this work. Large and negative mass renormalization indicates that for $r_s \gg 1$ the system goes into a correlated regime.

2. κ as a control parameter

Let us recapitulate first that we focus on the *extrinsic* monolayer graphene system here, that is $k_F > 0$. This is essentially a classical Fermi liquid in marked contrast to the more complicated *intrinsic* graphene $k_F = 0$. For the latter we refer to a comprehensive summary by Tang *et al.* [91]. While many conceptual problems do not arise in the extrinsic case, some important insight can be obtained from the intrinsic graphene. Consider for instance the expression for the Fermi velocity renormalization derived in Ref. [90] and plotted in Fig. 21 (left) as dotted lines:

$$\frac{v_F^* - v_F}{v_F} = -\frac{\alpha}{\pi} \left(\frac{5}{3} + \log \alpha \right) + \frac{\alpha}{4} \log \left(\frac{k_c}{k_F} \right). \quad (97)$$

Here the first part is extrinsic. It describes scattering processes in which the initial and the final state belong to the same band $s = s' = 1$ and contains no adjustable parameters. The second part is intrinsic, it includes scattering processes changing the band $s = -s' = 1$ and therefore depends on the momentum cutoff. In going to higher perturbative orders, such as including $\Sigma_{a\bar{a}}$, more and more processes involve interband scatterings and the role of intraband scattering is diminishing (as explicitly demonstrated for BLG, Fig. 17).

Let us inspect the qualitative dependence of the renormalized velocity on the interaction parameter $\alpha \simeq 2.2/\kappa$ (55). At higher α , the dependence deviates from linear. This is already evident from the extrinsic part in Eq. (97). The intrinsic part shows a similar trend when computed beyond the leading

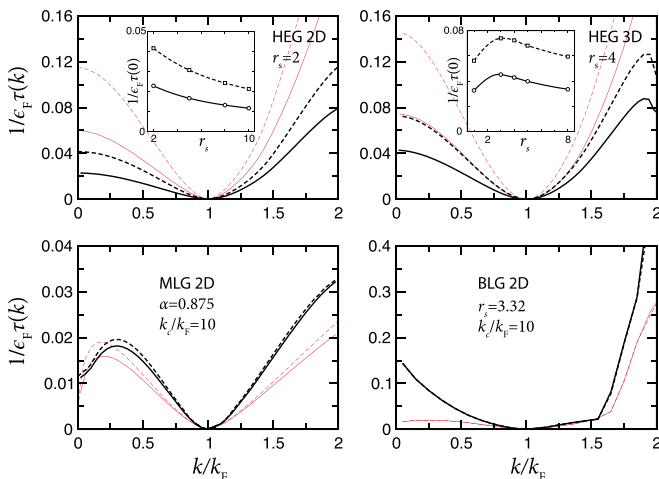


FIG. 22. Inverse quasiparticle lifetime (90) as a function of momentum. In the two insets, the values at the band bottom $\tau(k=0)^{-1}$ is shown for different r_s . Red lines additionally show the on-shell approximation (99) without (dashed) and with (full) $\Sigma_{a\bar{a}}$.

order [91]. By consistently including other terms, one can improve the agreement of asymptotic theory with our numerical results.

Generally, it is believed that G_0W_0 results are already very accurate [63]. However, higher-order diagrams have been treated in Ref. [71] and quantum Monte Carlo calculations were performed in Ref. [91]. All of them are concerned with the intrinsic case, which is still relevant to some extent as stated above, however cannot be used for a direct comparison. They predict a slightly larger velocity renormalization, whereas we observe here that the inclusion of $\Sigma_{a\bar{a}}$ leads to smaller values, Fig. 21.

3. Quasiparticle lifetime

$1/\tau(k)$ is an essential ingredient of the quasiparticle spectral function (86). We determine it by solving the Dyson equation in the complex frequency plane. Also, it can be obtained from the Fermi golden rule as advocated by Qian and Vignale [17]. From the discussion in Sec. II we know that the two are completely equivalent.

In Fig. 22 we summarize our finding for $\tau(k)$ computed for $0 < k < 2k_F$. In many studies, the ‘‘on-shell’’ imaginary self-energy is taken as a measure of the inverse lifetime

$$\tau(k)^{-1} = -\text{Im} \Sigma^R[k, \epsilon(k)], \quad (98)$$

where $\epsilon(k)$ is the bare dispersion relation. Apart from missing the Z_{qp} prefactor, this approach is reasonable for $k \approx k_F$, where the difference between the ‘‘true’’ $\epsilon_{qp}(k)$ and the bare $\epsilon(k)$ spectrum is small. For $\xi_k = |\epsilon(k) - \epsilon_F|/\epsilon_F \gg 1$ the difference between Eq. (89) and the on-shell approximation (98) is substantial, as can be seen by comparing black and red lines in Fig. 22. We find, for instance for MLG, that the approximation incorrectly yields vanishing scattering rates at the Dirac point ($k=0$). One consequence of this is the diverging inelastic mean free path at zero temperature predicted in Ref. [92]. On the other hand, Eq. (89) yields a finite value. It is worth noting that for the two HEG systems the correction upon the on-shell value is mostly associated with

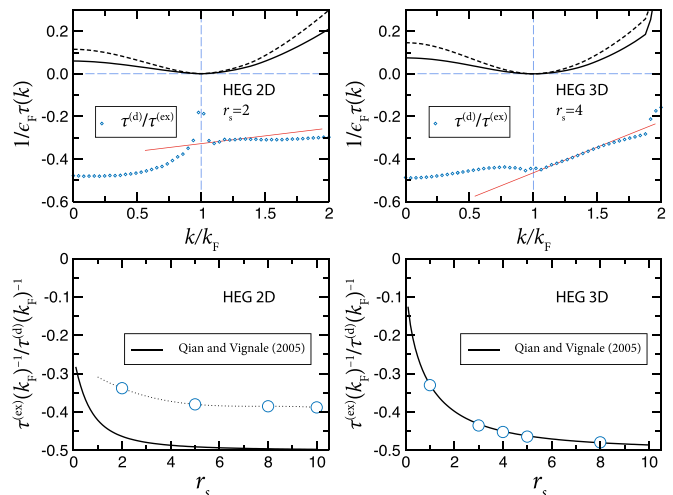


FIG. 23. Top row: Determination of the ratio $\tau^{(\text{ex})}(k)^{-1}/\tau^{(\text{d})}(k)^{-1}$ for the homogeneous electron gas in 2D and 3D illustrating numerical difficulties of taking the $k \rightarrow k_F$ limit. Bottom row: Comparison with analytical results of Ref. [17]: $\zeta_n^{(\text{ex})}(r_s)/\zeta_n^{(\text{d})}(r_s)$, see Eqs. (101) and (102).

the quasiparticle strength Z_{qp} renormalization, whereas for graphene systems (MLG and BLG) the deviation of $\epsilon_{qp}(k)$ from $\epsilon(k)$ also plays a role.

Only for the two HEG systems the impact of $\Sigma_{a\bar{a}}$ is appreciable as depicted in the insets of Fig. 22 for $\tau(0)^{-1}$ for different r_s values. The dependence is not always monotonic. For $\xi_k \ll 1$ we can compare with the asymptotic expressions from Ref. [45]:

$$\frac{1}{\tau(k)} = \frac{1}{4\pi} \zeta_2(r_s) \xi_k^2 \log\left(\frac{4}{\xi_k}\right), \quad 2\text{D}, \quad (99)$$

$$\frac{1}{\tau(k)} = \frac{\pi}{8} \zeta_3(r_s) \xi_k^2, \quad 3\text{D}. \quad (100)$$

They have shown that the inclusion of exchange modifies the density-dependent prefactors ζ_n without affecting the functional form. However, the fitting of small values with this form is not a trivial task because of (i) numerical issues and (ii) our insufficient knowledge of the subleading terms.³ We follow Qian and Vignale [17], where the coefficients $\zeta_n(r_s)$ are derived:

$$\zeta_2(r_s) = \left[1 + \frac{1}{2} \frac{\alpha_2^2 r_s^2}{(1 + \alpha_2 r_s)^2} \right] - \left[\frac{1}{4} + \frac{1}{2} \frac{\alpha_2 r_s}{1 + \alpha_2 r_s} \right], \quad (101)$$

$$\zeta_3(r_s) = \frac{1}{2\lambda} \left[\tan^{-1} \lambda + \frac{\lambda}{1 + \lambda^2} \right] - \frac{1}{2\lambda} \left[\frac{1}{\sqrt{2 + \lambda^2}} \cot^{-1} \frac{1}{\lambda \sqrt{2 + \lambda^2}} \right], \quad (102)$$

with $\lambda = \pi^{1/2}/(\alpha_3 r_s)^{1/2}$. Here the first brackets originate from the direct (d) processes and the second from the exchange (ex). In Fig. 23 we determine the ratio of exchange to direct scattering rates using the on-shell approximation (99) with $\Sigma_{a\bar{a}}$ and $\Sigma_{G_0W_0}$, respectively. In 3D the agreement with the analytical results (100) is very good, whereas in 2D we find

³In 2D, there are disagreements in the subleading terms [17,93,94].

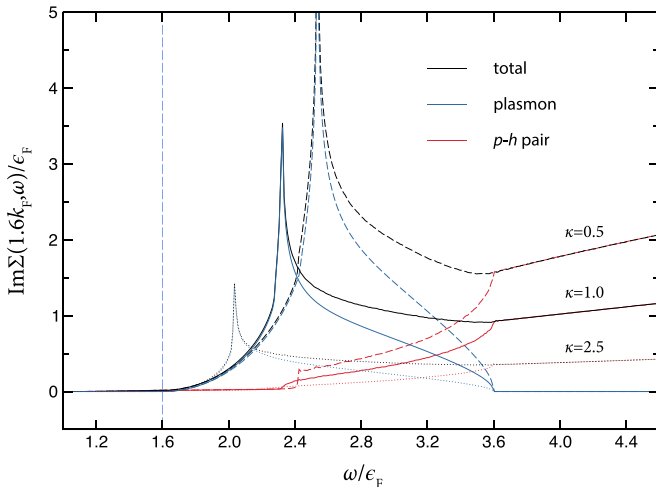


FIG. 24. Imaginary self-energy part of MLG for different interaction strengths. The on-shell value is only weakly dependent on κ in agreement with the analytical result of Polini and Vignale [95].

that the ratio is smaller. One possible explanation of this discrepancy could be the absence of the plasmonic contributions to the direct scattering in Ref. [17]. Besides ratios, we also compared absolute values with analytical predictions and found systematic underestimates. However, this should not be a surprise because the theory only yields the leading terms.

For MLG, the inverse lifetime follows the same asymptotic with famous logarithmic correction [57] as for the HEG 2D, Eq. (99) [92]. Polini and Vignale provided a very pedagogical derivation of this fact [95], however, exchange contributions were not included. Our simulations show that they are indeed small for MLG and BLG systems, Fig. 22. One interesting conclusion of Ref. [95] is that the scatterings are dominated by the “collinear scattering singularity,” that is, the momenta of electrons involved in the scattering are mostly parallel to each other. We find it interesting because of its apparent similarities with the scattering processes shaping Σ_{2x} , see our analysis in Sec. VB. Another interesting conclusion of the analytical formula is that the lifetime is independent of the dielectric constant. While our numerics shows that its only approximately true for full-fledged calculations using Eq. (89), an illustration on why this is the case for the on-shell τ^{-1} is provided in Fig. 24. There we plot the imaginary self-energy part for $k = 1.6k_F$ and three different dielectric constants $\kappa = 0.5, 1.0, 2.5$ resolving plasmonic and p - h contributions. Approaching the “on-shell” frequency marked as a vertical dashed line, the curves essentially fall on top of each other. The figure also illustrates the difficulties of the numerical determination of the asymptotic prefactors in Eq. (99) (for MLG they also depend on the momentum cutoff).

VI. CONCLUSIONS

Hedin’s set of functional equations allows us to expand the electron self-energy in terms of dressed G and W . The first term of such an expansion—the GW approximation—has been successfully applied to many systems. However, there are cases when this approximation is insufficient and higher-order terms need to be taken into account. One such

approximation has been derived in our previous work starting from the first- and second-order SE [4]. $\Sigma_{aa} + [\Sigma_{cc} + \Sigma_{c\bar{c}}] + \Sigma_{a\bar{a}}$ describes three distinct scattering processes in many-body systems, comprises all the first- and second-order terms and a subset of third and fourth order terms, and, crucially, has the PSD property [6]. In this work we focused on $\Sigma_{a\bar{a}}$, relevant for small energy transfers, and evaluated it in the quasiparticle approximation for the electron GF and RPA for the screened interaction. We found that screening is important and must be determined consistently. For inconsistent screening, unphysical singularities have been observed in Σ_{2x} , which is the bare Coulomb limit of $\Sigma_{a\bar{a}}$. Nonetheless, Σ_{2x} provides important corrections to the total energy in full agreement with analytic results of Onsager *et al.* [66].

We conducted a comprehensive investigation of the impact of $\Sigma_{a\bar{a}}$ on quasiparticle properties of the homogeneous electron gas in 2D and 3D, and of the mono- and bilayer graphene. The quasiparticle renormalization factor $Z_{qp}(k_F)$, the effective mass m^* , the Fermi velocity v_F^* , and the quasiparticle lifetime $\tau(k)$ have been computed for a range of interaction strengths controlled by the density r_s or the dielectric function κ . In the weakly correlated limit ($r_s \ll 1$ or $\kappa \gg 1$) we compared with asymptotic expansions, and in the correlated regime with results of other theories such as quantum Monte Carlo and perturbative calculations including local field factors.

It is known that exchange processes encoded in $\Sigma_{a\bar{a}}$ reduce the quasiparticle scattering rate. This has been shown in the asymptotic limit $\omega \rightarrow \infty$ by Vogt *et al.* [69] and in the vicinity of k_F by Qian and Vignale [17]. Besides confirming this finding using a completely different methodology (asymptotic results in Fig. 15, quasiparticle lifetimes in Fig. 22), we also observed an appreciable effect of $\Sigma_{a\bar{a}}$ on the effective mass m^* and quasiparticle strength Z_{qp} in the 3D HEG.

However, the effect of $\Sigma_{a\bar{a}}$ is rather small in the 2D HEG (see Figs. 19 and 20). This is rather unexpected. Together with the high indeterminacy of the Monte Carlo simulations [73,82] for this system and the high relevance of this model for prospective materials [36,96], it calls for further investigations. We have also shown that the effect is small for extrinsic graphene systems. However, this was anticipated on the basis of other studies [28,41,48]. There are currently no calculations for graphene with local field factors. Given their good performance and robustness for the 2D [75] and 3D [76] HEG and connections with the density-functional concept [97], it would be interesting to see how these methods perform for MLG and BLG.

We further note that $\Sigma_{a\bar{a}}$ is only one of many scattering processes taking place in correlated many-body systems. Being operative in the vicinity of a quasiparticle peak, it is important for the description of transport properties such as the effective mass m^* and quasiparticle lifetimes. Other diagrams, for instance $\Sigma_{c\bar{c}}$, are important for the *off-shell* spectroscopic properties, e.g., second plasmonic satellites [8,10,32,35]. Dedicated methods based on the cumulant expansion [33,34,37,38] can describe them at the reduced numerical cost. The very fact that different diagrams are operative in distinct spectral ranges [6,29] and contribute additively to the scattering rate $\Gamma(k, \omega)$ makes it possible to separately consider these effects.

Although we have focused on one particular scattering process, the PSD diagrammatic construction is versatile and

applicable to realistic multiband systems. Furthermore, the PSD diagrams remain PSD upon replacement of the zero-temperature Green's function with the finite-temperature [98] or any excited-state Green's function. This latter possibility opens the way towards the systematic inclusion of vertex corrections in the spectral function of systems in a (quasi) steady state. Investigations in the field of, e.g., molecular transport and time-resolved (tr) and angle-resolved photoemission spectroscopy (ARPES), are therefore foreseeable in the near future. The spectral function is indeed a key quantity to determine the conductance of atomic-scale junctions, and MBPT calculations have so far been limited to the *GW* [99–103] and second-Born [102,103] approximation. Similarly, the tr-ARPES signal is related to the transient spectral function [104,105] which in semiconductor or insulators can be evaluated using a steady-state approximation (provided that the carrier relaxation time is much longer than the probe pulse). In this context [106] the PSD diagrammatic construction may provide a powerful tool in the field of light-induced exciton fluids, whose incoherent plasma phase [105,107,108] and coherent condensed phase [96,109–114] are currently under intense investigations.

ACKNOWLEDGMENTS

We thank A.-M. Uimonen for useful discussions. The work has been performed under the Project HPC-EUROPA3 (INFRAIA-2016-1-730897), with the support of the EC Research Innovation Action under the H2020 Programme; in particular, Y.P. gratefully acknowledges the computer resources and technical support provided the CSC-IT Center for Science (Espoo, Finland). Y.P. acknowledges support of Deutsche Forschungsgemeinschaft (DFG), Collaborative Research Centre SFB/TRR 173 “Spin+X.” G.S. acknowledges funding from MIUR PRIN Grant No. 20173B72NB and from INFN17_nemesys project. R.v.L. likes to thank the Academy of Finland for support under Grant No. 317139.

APPENDIX A: HILBERT TRANSFORM AND SPECTRAL FUNCTIONS

The Hilbert transform is an important part of our numerical procedure. We define

$$H[x](t) = \frac{1}{\pi} \mathcal{P} \int_{-\infty}^{\infty} d\tau \frac{x(\tau)}{t - \tau}. \quad (\text{A1})$$

It has the properties $H[H[x]](t) = -x(t)$, $H^{-1}[x](t) = -H[x](t)$, and is computed using FFT. In particular we need the relation between the real part of the correlation self-energy and the rate function $\Gamma(k, \omega)$, Eq. (1), which in our approach is computed by the Monte Carlo method,

$$\text{Re } \Sigma_c^R(k, \omega) = \frac{1}{2} H[\Gamma(k)](\omega), \quad (\text{A2})$$

$$\frac{1}{2} \Gamma(k, \omega) = -\text{Im } \Sigma_c^R(k, \omega). \quad (\text{A3})$$

There are the following possibilities to obtain positive spectral functions starting from the second-order self-energy:

$$\mp i \Sigma_{aa}^{\lessgtr}(k, \omega) \geq 0, \quad (\text{A4a})$$

$$\mp i (\Sigma_{cc}^{\lessgtr} + \Sigma_{cc}^{\lessgtr})(k, \omega) \geq 0, \quad (\text{A4b})$$

$$\mp i (\Sigma_{aa}^{\lessgtr} + \Sigma_{aa}^{\lessgtr})(k, \omega) \geq 0. \quad (\text{A4c})$$

Consequently, the sum of all contributions given by Eq. (8) is also PSD. By using the method from our earlier work [4], these results can also be generalized to any dressed GFs that possess a positive spectral function.

APPENDIX B: EQUILIBRIUM PROPAGATORS

We define the bare electron propagators as averages of the field operators in the Heisenberg picture over the noninteracting state

$$g^<(1, 2) = i \langle \hat{\psi}_H^\dagger(2) \hat{\psi}_H(1) \rangle_0, \\ g^>(1, 2) = -i \langle \hat{\psi}_H(1) \hat{\psi}_H^\dagger(2) \rangle_0,$$

fulfilling the symmetry relations

$$i g^{\lessgtr}(1, 2) = [i g^{\lessgtr}(2, 1)]^*. \quad (\text{B1})$$

Analogously, the density-density correlators are defined with respect to the interacting ground state

$$\chi^>(1, 2) = -i \langle \Delta \hat{n}_H(1) \Delta \hat{n}_H(2) \rangle, \\ \chi^<(1, 2) = -i \langle \Delta \hat{n}_H(2) \Delta \hat{n}_H(1) \rangle,$$

with the density deviation $\Delta \hat{n}_H(1) = \hat{n}_H(1) - \langle \hat{n}_H(1) \rangle$. They fulfill the symmetries

$$i \chi^{\lessgtr}(1, 2) = [i \chi^{\lessgtr}(2, 1)]^*. \quad (\text{B2})$$

Because the screened interaction is directly related to χ ,

$$W(1, 2) = v(1, 2) + \iint d(3, 4) v(1, 3) \chi(3, 4) v(4, 3), \quad (\text{B3})$$

all the symmetry and analytic properties also hold for W .

For homogeneous systems the momentum-energy representation is useful, which we formulate here in Fermi units (k_F, ϵ_F). The Kubo-Martin-Schwinger conditions allow us to write the lesser/greater propagators in terms of the retarded ones,

$$g^<(x, \zeta) = -2i n_F(\zeta) \text{Im } g^R(x, \zeta), \quad (\text{B4a})$$

$$g^>(x, \zeta) = -2i (n_F(\zeta) - 1) \text{Im } g^R(x, \zeta); \quad (\text{B4b})$$

$$W_0^<(y, \xi) = +2i n_B(\xi) \text{Im } W_0^R(y, \xi), \quad (\text{B4c})$$

$$W_0^>(y, \xi) = +2i [n_B(\xi) + 1] \text{Im } W_0^R(y, \xi). \quad (\text{B4d})$$

$n_{F/B}$ are the Fermi/Bose distribution functions, which at zero temperature reduce to simple step-functions

$$n_F(\zeta) = \theta(1 - \zeta), \quad \bar{n}_F(\zeta) = 1 - n_F(\zeta); \quad (\text{B5a})$$

$$n_B(\xi) = -\theta(-\xi) = \theta(\xi) - 1, \quad n_B(\xi) + 1 = \theta(\xi). \quad (\text{B5b})$$

For the bare propagators we furthermore have

$$g^R(x, \zeta) = \frac{1}{\zeta - \epsilon(x) + i\eta}, \quad (\text{B6})$$

and we use a spectral representation of the screened interaction

$$W_0^R(y, \xi) = v(y) + \int_0^\infty d\omega \frac{2\omega C(y, \xi)}{(\xi + i\eta)^2 - \omega^2}, \quad (\text{B7})$$

where $v(y)$ is the bare Coulomb interaction. It fulfills the symmetry property

$$[W_0^R(y, \xi)]^* = W_0^R(y, -\xi). \quad (\text{B8})$$

Comparing it with the Hilbert transform of the inverse dielectric function

$$\frac{1}{\varepsilon^R(y, \xi)} = 1 - \int_0^\infty \frac{d\omega}{\pi} \text{Im} \left[\frac{1}{\varepsilon^R(y, \omega)} \right] \frac{2\omega}{(\xi + i\eta)^2 - \omega^2}, \quad (\text{B9})$$

we have for the spectral function of the continuous spectrum

$$C(y, \omega) = v(y) \text{Im} \left[-\frac{1}{\pi} \frac{1}{\varepsilon^R(y, \omega)} \right], \quad (\text{B10})$$

and for plasmons $C(y, \omega) = C(y)\delta[\omega - \Omega(y)]$ with

$$C(y) = v(y) \left[\frac{\partial \text{Re} \varepsilon^R(y, \xi)}{\partial \xi} \Big|_{\xi=\Omega(y)} \right]^{-1}. \quad (\text{B11})$$

The time-ordered ($W_0^T \equiv W_0^{--}$) and the anti-time-ordered ($W_0^{\bar{T}} \equiv W_0^{++}$) screened interactions read

$$W_0^T(y, \xi) = v(y) + \int_0^\infty d\omega \frac{2\omega C(y, \omega)}{\xi^2 - (\omega - i\eta)^2}, \quad (\text{B12})$$

$$W_0^{\bar{T}}(y, \xi) = -[W_0^T(y, \xi)]^*, \quad (\text{B13})$$

with $W_0^T(y, -\xi) = W_0^{\bar{T}}(y, \xi)$.

APPENDIX C: POLARIZABILITY OF MLG

The dynamical polarization of graphene at finite doping has been computed by Hwang and Das Sarma [49] and by Wunsch *et al.* [50]. We present here for completeness the functions G_r ,

$$G_r(y, \xi) = \begin{cases} 0 & 1A \\ \pi + G_<(z_1) & 2A \\ \pi + G_<(z_1) + G_<(z_2) & 3A \\ -G_>(z_2) + G_>(-z_1) & 1B \\ -G_>(z_2) & 2B \\ -G_>(z_2) + G_>(z_1) & 3B \end{cases} \quad (\text{C1})$$

and G_i ,

$$G_i(y, \xi) = \begin{cases} G_>(z_2) - G_>(-z_1) & 1A \\ G_>(z_2) & 2A \\ 0 & 3A \\ 0 & 1B \\ \pi + G_<(z_1) & 2B \\ \pi & 3B \end{cases} \quad (\text{C2})$$

that define the dielectric function in Eqs. (56) and (58) with

$$z_1 = \frac{\xi - 2}{y}, \quad z_2 = \frac{\xi + 2}{y}, \quad (\text{C3})$$

and

$$G_>(z) = z\sqrt{z^2 - 1} - \text{arccosh}(z), \quad (\text{C4})$$

$$G_<(z) = z\sqrt{1 - z^2} - \arccos(z). \quad (\text{C5})$$

Notice that A domains are for $\xi < y$ and B domains are for $\xi > y$ as shown in Fig. 5.

APPENDIX D: POLARIZABILITY OF BLG

We start by defining the four critical lines

$$r_1 = y^2 + 2y + \xi + 2; \quad r_2 = y^2 + \xi;$$

$$r_3 = y^2 - 2y + \xi + 2; \quad r_4 = \frac{y^2}{2} + \xi.$$

Furthermore, we introduce some auxiliary functions:

$$q_1 = \frac{y^2 - 2\xi}{4\xi} \log 2 + \frac{r_4}{2\xi} \log |r_4| - \frac{r_2}{2\xi} \log |r_2| \theta(y - 1) + \left(\frac{r_2}{4\xi} \log |1 + \xi| + \frac{y^2}{4\xi} \log |y^2| \right) \text{sgn}(y - 1), \quad (\text{D1})$$

$$q_2 = \left[\frac{|r_2|}{4\xi} \log \left| \frac{(2 + \xi)\sqrt{r_2 r_2} + \xi\sqrt{r_1 r_3}}{(2 + \xi)\sqrt{r_2 r_2} - \xi\sqrt{r_1 r_3}} \right| - \frac{1}{4} \log \left| \frac{\sqrt{r_1 r_3} + 2 + \xi}{\sqrt{r_1 r_3} - (2 + \xi)} \right| \right] [\theta(-r_1) - \theta(r_3)], \quad (\text{D2})$$

$$p_1 = \left[\frac{r_2}{2\xi} \arctan \left(\frac{(2 + \xi)r_2}{\xi\sqrt{-r_1 r_3}} \right) + \frac{1}{2} \arccos \left(\frac{2 + \xi}{y\sqrt{-2r_4}} \right) \right] \theta(-r_1 r_3), \quad (\text{D3})$$

$$p_2 = \frac{\pi r_2}{4\xi} \text{sgn}(r_2) \theta(-r_1 r_3) + \frac{\pi r_4}{\xi} \theta(y - 2) \theta(-r_4) \theta(r_3) - \frac{\pi y^2}{2\xi} \theta(-r_1). \quad (\text{D4})$$

With the help of these definitions

$$\text{Re} \Pi_2(y, \xi) = q_1 + q_2; \quad \text{Im} \Pi_2(y, \xi) = p_1 + p_2. \quad (\text{D5})$$

APPENDIX E: SOLUTION OF THE DYSON EQUATION

Let us recapitulate possible approaches to the solution of the Dyson equation

$$G(k, \omega) = g(k, \omega) + g(k, \omega) \Sigma(k, \omega) G(k, \omega) \quad (\text{E1})$$

following Ref. [30]. In the preceding sections the self-energy is computed using bare propagators (B4) $\Sigma = \Sigma[g, W_0]$. This approach has an inherent problem that the $k = k_F$ state is *no longer a sharp quasiparticle state*. We still can improve the *one-shot* calculations by applying some rigid shift $\Delta\mu$ to all poles,

$$G_0(k, \omega) = \frac{1}{\omega - \epsilon_0(k) - \Delta\mu + i\eta} = g(k, \omega - \Delta\mu). \quad (\text{E2})$$

The respective self-energy then reads

$$\Sigma[G_0, W_0](k, \omega) = \Sigma[g, W_0](k, \omega - \Delta\mu), \quad (\text{E3})$$

allowing us to rewrite the quasiparticle approximation for the Dyson's equation

$$\epsilon(k) = \epsilon_0(k) + \Sigma[g, W_0][k, \epsilon(k) - \Delta\mu], \quad (\text{E4})$$

$$\tilde{\epsilon}(k) = \epsilon_0(k) - \Delta\mu + \Sigma[g, W_0][k, \tilde{\epsilon}(k)], \quad (\text{E5})$$

Thus, the quasiparticle approximation for G reads

$$G(k, \omega) = \frac{1}{\omega - \tilde{\epsilon}(k)}. \quad (\text{E6})$$

Now we demand that the solution of the Dyson equation at $k = k_F$ takes the form

$$G(k_F, \omega) = \frac{1}{\omega - \mu + i\eta} = G_0(k_F, \omega) \quad (\text{E7})$$

and coincides with the improved propagator G_0 (E2) representing a sharp quasiparticle peak at the chemical potential. The consistency condition (E7) provides the interpretation of $\Delta\mu$ as the correlation shift of the chemical potential

$$\Delta\mu = \mu - \epsilon_F, \quad (\text{E8})$$

and allows us to determine it. To this end we insert Eq. (E7) into Eq. (E4) leading to

$$\mu = \epsilon_F + \text{Re } \Sigma[G_0, W_0](k_F, \mu). \quad (\text{E9})$$

This point and the connection of μ to the *total energy per electron* is explained in Ref. [115] (p. 82). Combining Eq. (E8) with Eq. (E9) we obtain

$$\Delta\mu = \text{Re } \Sigma[g, W_0](k_F, \epsilon_F). \quad (\text{E10})$$

Thus, $\Delta\mu$ is expressed solely in terms of the self-energy for $k = k_F$ and $\omega = \epsilon_F$. In the case of MLG and BLG having two bands, one additionally sets the band index s consistent with the doping (typically the chemical potential is *above* the Dirac point implying $s = +1$).

-
- [1] L. Hedin, *Phys. Rev.* **139**, A796 (1965).
[2] P. Minnhagen, *J. Phys. C* **7**, 3013 (1974).
[3] P. Minnhagen, *J. Phys. C* **8**, 1535 (1975).
[4] G. Stefanucci, Y. Pavlyukh, A.-M. Uimonen, and R. van Leeuwen, *Phys. Rev. B* **90**, 115134 (2014).
[5] A.-M. Uimonen, G. Stefanucci, Y. Pavlyukh, and R. van Leeuwen, *Phys. Rev. B* **91**, 115104 (2015).
[6] Y. Pavlyukh, A.-M. Uimonen, G. Stefanucci, and R. van Leeuwen, *Phys. Rev. Lett.* **117**, 206402 (2016).
[7] B. Holm and U. von Barth, *Phys. Rev. B* **57**, 2108 (1998).
[8] J. M. Riley, F. Caruso, C. Verdi, L. B. Duffy, M. D. Watson, L. Bawden, K. Volckaert, G. van der Laan, T. Hesjedal, M. Hoesch, F. Giustino, and P. D. C. King, *Nat. Commun.* **9**, 2305 (2018).
[9] B. Holm and F. Aryasetiawan, *Phys. Rev. B* **56**, 12825 (1997).
[10] M. Guzzo, J. J. Kas, L. Sponza, C. Giorgetti, F. Sottile, D. Pierucci, M. G. Silly, F. Sirotti, J. J. Rehr, and L. Reining, *Phys. Rev. B* **89**, 085425 (2014).
[11] D. C. Langreth, *Phys. Rev. B* **1**, 471 (1970).
[12] Y. Pavlyukh, *Sci. Rep.* **7**, 504 (2017).
[13] K. Balzer, S. Bauch, and M. Bonitz, *Phys. Rev. A* **82**, 033427 (2010).
[14] E. Perfetto, A.-M. Uimonen, R. van Leeuwen, and G. Stefanucci, *Phys. Rev. A* **92**, 033419 (2015).
[15] M. Schüler and Y. Pavlyukh, *Phys. Rev. B* **97**, 115164 (2018).
[16] P. Ziesche, *Ann. Phys.* **16**, 45 (2007).
[17] Z. Qian and G. Vignale, *Phys. Rev. B* **71**, 075112 (2005).
[18] C.-O. Almbladh, *J. Phys.: Conf. Ser.* **35**, 127 (2006).
[19] Y. Pavlyukh, M. Schüler, and J. Berakdar, *Phys. Rev. B* **91**, 155116 (2015).
[20] M. Schüler, Y. Pavlyukh, P. Bolognesi, L. Avaldi, and J. Berakdar, *Sci. Rep.* **6**, 24396 (2016).
[21] A. Grüneis, M. Marsman, J. Harl, L. Schimka, and G. Kresse, *J. Chem. Phys.* **131**, 154115 (2009).
[22] X. Ren, N. Marom, F. Caruso, M. Scheffler, and P. Rinke, *Phys. Rev. B* **92**, 081104(R) (2015).
[23] B. I. Lundqvist, *Phys. Kondens. Mater.* **7**, 117 (1968).
[24] G. E. Santoro and G. F. Giuliani, *Phys. Rev. B* **39**, 12818 (1989).
[25] E. H. Hwang and S. Das Sarma, *Phys. Rev. B* **77**, 081412(R) (2008).
[26] M. Polini, R. Asgari, G. Borghi, Y. Barlas, T. Pereg-Barnea, and A. H. MacDonald, *Phys. Rev. B* **77**, 081411(R) (2008).
[27] R. Sensarma, E. H. Hwang, and S. Das Sarma, *Phys. Rev. B* **84**, 041408(R) (2011).
[28] V. N. Kotov, B. Uchoa, V. M. Pereira, F. Guinea, and A. H. Castro Neto, *Rev. Mod. Phys.* **84**, 1067 (2012).
[29] Y. Pavlyukh, A. Rubio, and J. Berakdar, *Phys. Rev. B* **87**, 205124 (2013).
[30] G. Stefanucci and R. van Leeuwen, *Nonequilibrium Many-Body Theory of Quantum Systems: A Modern Introduction* (Cambridge University Press, Cambridge, 2013).
[31] G. Strinati, *Riv. Nuovo Cimento* **11**, 1 (1988).
[32] F. Aryasetiawan, L. Hedin, and K. Karlsson, *Phys. Rev. Lett.* **77**, 2268 (1996).
[33] J. J. Kas, J. J. Rehr, and L. Reining, *Phys. Rev. B* **90**, 085112 (2014).
[34] B. Gumhalter, V. Kovač, F. Caruso, H. Lambert, and F. Giustino, *Phys. Rev. B* **94**, 035103 (2016).
[35] C. Verdi, F. Caruso, and F. Giustino, *Nat. Commun.* **8**, 15769 (2017).
[36] F. Caruso, H. Lambert, and F. Giustino, *Phys. Rev. Lett.* **114**, 146404 (2015).
[37] M. Z. Mayers, M. S. Hybertsen, and D. R. Reichman, *Phys. Rev. B* **94**, 081109(R) (2016).
[38] J. McClain, J. Lischner, T. Watson, D. A. Matthews, E. Ronca, S. G. Louie, T. C. Berkelbach, and G. K.-L. Chan, *Phys. Rev. B* **93**, 235139 (2016).
[39] R. van Leeuwen and G. Stefanucci, *Phys. Rev. B* **85**, 115119 (2012).
[40] D. L. Freeman, *Phys. Rev. B* **15**, 5512 (1977).
[41] S. Das Sarma, S. Adam, E. H. Hwang, and E. Rossi, *Rev. Mod. Phys.* **83**, 407 (2011).
[42] D. N. Basov, M. M. Fogler, and F. J. Garcia de Abajo, *Science* **354**, aag1992 (2016).
[43] A. Czachor, A. Holas, S. R. Sharma, and K. S. Singwi, *Phys. Rev. B* **25**, 2144 (1982).
[44] F. Stern, *Phys. Rev. Lett.* **18**, 546 (1967).
[45] G. Giuliani and G. Vignale, *Quantum Theory of the Electron Liquid* (Cambridge University Press, Cambridge, UK, 2005).
[46] I. S. Gradshteyn and I. M. Ryzhik, *Table of Integrals, Series, and Products*, 7th ed. (Elsevier, Amsterdam, 2007).
[47] T. Ando, *J. Phys. Soc. Jpn.* **75**, 074716 (2006).
[48] D. N. Basov, M. M. Fogler, A. Lanzara, F. Wang, and Y. Zhang, *Rev. Mod. Phys.* **86**, 959 (2014).
[49] E. H. Hwang and S. Das Sarma, *Phys. Rev. B* **75**, 205418 (2007).

- [50] B. Wunsch, T. Stauber, F. Sols, and F. Guinea, *New J. Phys.* **8**, 318 (2006).
- [51] E. H. Hwang, R. E. Throckmorton, and S. Das Sarma, *Phys. Rev. B* **98**, 195140 (2018).
- [52] P. E. Trevisanutto, C. Giorgetti, L. Reining, M. Ladisa, and V. Olevano, *Phys. Rev. Lett.* **101**, 226405 (2008).
- [53] E. H. Hwang, B. Y.-K. Hu, and S. Das Sarma, *Phys. Rev. Lett.* **99**, 226801 (2007).
- [54] R. Sensarma, E. H. Hwang, and S. Das Sarma, *Phys. Rev. B* **82**, 195428 (2010).
- [55] E. H. Hwang and S. Das Sarma, *Phys. Rev. Lett.* **101**, 156802 (2008).
- [56] U. von Barth and B. Holm, *Phys. Rev. B* **54**, 8411 (1996).
- [57] G. F. Giuliani and J. J. Quinn, *Phys. Rev. B* **26**, 4421 (1982).
- [58] Y. Zhang and S. Das Sarma, *Phys. Rev. B* **71**, 045322 (2005).
- [59] J. Lischner, D. Vigil-Fowler, and S. G. Louie, *Phys. Rev. B* **89**, 125430 (2014).
- [60] A. Bostwick, F. Speck, T. Seyller, K. Horn, M. Polini, R. Asgari, A. H. MacDonald, and E. Rotenberg, *Science* **328**, 999 (2010).
- [61] A. L. Walter, A. Bostwick, K.-J. Jeon, F. Speck, M. Ostler, T. Seyller, L. Moreschini, Y. J. Chang, M. Polini, R. Asgari, A. H. MacDonald, K. Horn, and E. Rotenberg, *Phys. Rev. B* **84**, 085410 (2011).
- [62] J. P. Carbotte, J. P. F. LeBlanc, and E. J. Nicol, *Phys. Rev. B* **85**, 201411(R) (2012).
- [63] S. Das Sarma and E. H. Hwang, *Phys. Rev. B* **87**, 045425 (2013).
- [64] A. Sabashvili, S. Östlund, and M. Granath, *Phys. Rev. B* **88**, 085439 (2013).
- [65] M. L. Glasser and G. Lamb, *J. Phys. A* **40**, 1215 (2007).
- [66] L. Onsager, L. Mittag, and M. J. Stephen, *Ann. Phys.* **473**, 71 (1966).
- [67] A. Ishihara and L. Ioriatti, *Phys. Rev. B* **22**, 214 (1980).
- [68] M. L. Glasser, in *Many-body Approaches at Different Scales*, edited by G. Angilella and C. Amovilli (Springer International, Cham, 2018), pp. 291–296.
- [69] M. Vogt, R. Zimmermann, and R. J. Needs, *Phys. Rev. B* **69**, 045113 (2004).
- [70] J. González, F. Guinea, and M. A. H. Vozmediano, *Phys. Rev. B* **59**, R2474 (1999).
- [71] E. Barnes, E. H. Hwang, R. E. Throckmorton, and S. Das Sarma, *Phys. Rev. B* **89**, 235431 (2014).
- [72] A. V. Chubukov, *Phys. Rev. B* **48**, 1097 (1993).
- [73] M. Holzmann, B. Bernu, V. Olevano, R. M. Martin, and D. M. Ceperley, *Phys. Rev. B* **79**, 041308(R) (2009).
- [74] M. Holzmann, B. Bernu, C. Pierleoni, J. McMinis, D. M. Ceperley, V. Olevano, and L. Delle Site, *Phys. Rev. Lett.* **107**, 110402 (2011).
- [75] R. Asgari, B. Davoudi, M. Polini, G. F. Giuliani, M. P. Tosi, and G. Vignale, *Phys. Rev. B* **71**, 045323 (2005).
- [76] G. E. Simion and G. F. Giuliani, *Phys. Rev. B* **77**, 035131 (2008).
- [77] C. A. Kukkonen and A. W. Overhauser, *Phys. Rev. B* **20**, 550 (1979).
- [78] A. L. Kutepov and G. Kotliar, *Phys. Rev. B* **96**, 035108 (2017).
- [79] R. Sensarma, E. H. Hwang, and S. Das Sarma, *Phys. Rev. B* **86**, 079912(E) (2012).
- [80] E. Daniel and S. H. Vosko, *Phys. Rev.* **120**, 2041 (1960).
- [81] V. M. Galitski and S. Das Sarma, *Phys. Rev. B* **70**, 035111 (2004).
- [82] N. D. Drummond and R. J. Needs, *Phys. Rev. B* **80**, 245104 (2009).
- [83] M. Gell-Mann, *Phys. Rev.* **106**, 369 (1957).
- [84] G. Mahan, *Many-particle Physics*, 3rd ed. (Kluwer Academic/Plenum, New York, 2000).
- [85] J. F. Janak, *Phys. Rev.* **178**, 1416 (1969).
- [86] C. S. Ting, T. K. Lee, and J. J. Quinn, *Phys. Rev. Lett.* **34**, 870 (1975).
- [87] T. Ando, A. B. Fowler, and F. Stern, *Rev. Mod. Phys.* **54**, 437 (1982).
- [88] D. S. Saraga and D. Loss, *Phys. Rev. B* **72**, 195319 (2005).
- [89] F. G. Eich, M. Holzmann, and G. Vignale, *Phys. Rev. B* **96**, 035132 (2017).
- [90] S. Das Sarma, E. H. Hwang, and W.-K. Tse, *Phys. Rev. B* **75**, 121406(R) (2007).
- [91] H.-K. Tang, J. N. Leaw, J. N. B. Rodrigues, I. F. Herbut, P. Sengupta, F. F. Assaad, and S. Adam, *Science* **361**, 570 (2018).
- [92] Q. Li and S. Das Sarma, *Phys. Rev. B* **87**, 085406 (2013).
- [93] L. Zheng and S. Das Sarma, *Phys. Rev. B* **53**, 9964 (1996).
- [94] M. Reizer and J. W. Wilkins, *Phys. Rev. B* **55**, R7363 (1997).
- [95] M. Polini and G. Vignale, in *No-Nonsense Physicist: An Overview of Gabriele Giuliani's Work and Life*, edited by M. Polini, G. Vignale, V. Pellegrini, and J. K. Jain (Edizioni della Normale, Pisa, 2016).
- [96] D. Christiansen, M. Selig, E. Malic, R. Ernstorfer, and A. Knorr, *Phys. Rev. B* **100**, 205401 (2019).
- [97] F. Bruneval, F. Sottile, V. Olevano, R. Del Sole, and L. Reining, *Phys. Rev. Lett.* **94**, 186402 (2005).
- [98] J. J. Kas and J. J. Rehr, *Phys. Rev. Lett.* **119**, 176403 (2017).
- [99] K. S. Thygesen and A. Rubio, *J. Chem. Phys.* **126**, 091101 (2007).
- [100] C. D. Spataru, M. S. Hybertsen, S. G. Louie, and A. J. Millis, *Phys. Rev. B* **79**, 155110 (2009).
- [101] J. B. Neaton, M. S. Hybertsen, and S. G. Louie, *Phys. Rev. Lett.* **97**, 216405 (2006).
- [102] P. Myöhänen, A. Stan, G. Stefanucci, and R. van Leeuwen, *Europhys. Lett.* **84**, 67001 (2008).
- [103] P. Myöhänen, A. Stan, G. Stefanucci, and R. van Leeuwen, *Phys. Rev. B* **80**, 115107 (2009).
- [104] J. K. Freericks, H. R. Krishnamurthy, and T. Pruschke, *Phys. Rev. Lett.* **102**, 136401 (2009).
- [105] E. Perfetto, D. Sangalli, A. Marini, and G. Stefanucci, *Phys. Rev. B* **94**, 245303 (2016).
- [106] M. Hyrkäs, D. Karlsson, and R. van Leeuwen, *Phys. Status Solidi B* **256**, 1800615 (2019).
- [107] D. Semkat, F. Richter, D. Kremp, G. Manzke, W.-D. Kraeft, and K. Henneberger, *Phys. Rev. B* **80**, 155201 (2009).
- [108] A. Steinhoff, M. Florian, M. Rösner, G. Schönhoff, T. O. Wehling, and F. Jahnke, *Nat. Commun.* **8**, 1166 (2017).
- [109] A. Rustagi and A. F. Kemper, *Phys. Rev. B* **97**, 235310 (2018).

- [110] A. Rustagi and A. F. Kemper, *Phys. Rev. B* **99**, 125303 (2019).
- [111] E. Perfetto, D. Sangalli, A. Marini, and G. Stefanucci, *Phys. Rev. Mater.* **3**, 124601 (2019).
- [112] E. Perfetto, S. Bianchi, and G. Stefanucci, *Phys. Rev. B* **101**, 041201(R) (2020).
- [113] R. Hanai, P. B. Littlewood, and Y. Ohashi, *J. Low Temp. Phys.* **183**, 127 (2016).
- [114] K. W. Becker, H. Fehske, and V.-N. Phan, *Phys. Rev. B* **99**, 035304 (2019).
- [115] L. Hedin and S. Lundqvist, in *Solid State Physics*, edited by D. T. Frederick Seitz and H. Ehrenreich (Academic, New York, 1970), Vol. 23, pp. 1–181.